



Site U1592¹

Contents

- [1 Background and objectives](#)
- [3 Operations](#)
- [5 Lithostratigraphy](#)
- [18 Stratigraphic correlation](#)
- [21 Structural geology](#)
- [24 Biostratigraphy](#)
- [33 Paleomagnetism](#)
- [37 Physical properties](#)
- [42 Geochemistry](#)
- [46 References](#)

Keywords

International Ocean Discovery Program, IODP, R/V *JOIDES Resolution*, Expedition 398, Hellenic Arc Volcanic Field, Earth Connections, Earth in Motion, Biosphere Frontiers, Site U1592, Santorini caldera, Aegean Sea, Christiana-Santorini-Kolumbo volcanic field, subduction zone, shallow-marine volcanism

Core descriptions

Supplementary material

References (RIS)

MS 398-106

Published 30 July 2024

Funded by NSF OCE1326927, ECORD, and JAMSTEC

S. Kutterolf, T.H. Druitt, T.A. Ronge, S. Beethe, A. Bernard, C. Berthod, H. Chen, S. Chiyonobu, A. Clark, S. DeBari, T.I. Fernandez Perez, R. Gertisser, C. Hübscher, R.M. Johnston, C. Jones, K.B. Joshi, G. Kletetschka, O. Koukousioura, X. Li, M. Manga, M. McCanta, I. McIntosh, A. Morris, P. Nomikou, K. Pank, A. Peccia, P.N. Polymenakou, J. Preine, M. Tominaga, A. Woodhouse, and Y. Yamamoto²

¹ Kutterolf, S., Druitt, T.H., Ronge, T.A., Beethe, S., Bernard, A., Berthod, C., Chen, H., Chiyonobu, S., Clark, A., DeBari, S., Fernandez Perez, T.I., Gertisser, R., Hübscher, C., Johnston, R.M., Jones, C., Joshi, K.B., Kletetschka, G., Koukousioura, O., Li, X., Manga, M., McCanta, M., McIntosh, I., Morris, A., Nomikou, P., Pank, K., Peccia, A., Polymenakou, P.N., Preine, J., Tominaga, M., Woodhouse, A., and Yamamoto, Y., 2024. Site U1592. In Druitt, T.H., Kutterolf, S., Ronge, T.A., and the Expedition 398 Scientists, Hellenic Arc Volcanic Field. *Proceedings of the International Ocean Discovery Program, 398*. College Station, TX (International Ocean Discovery Program). <https://doi.org/10.14379/iodp.proc.398.106.2024>

² [Expedition 398 Scientists' affiliations.](#)

1. Background and objectives

Site U1592 (proposed Site CSK-09A) is located ~10 km southeast of Anhydros Island in the Anafi Basin at 693 meters below sea level (mbsl) (Figure F1). The aim at the site was to penetrate the entire volcano-sedimentary fill as far as the Alpine basement to reconstruct the evolution of the Anafi Basin: history of subsidence, presence of volcanic event layers in the basin sediments, and links between volcanism and crustal tectonics. We drilled to a maximum recovery depth of 519.8 meters below seafloor (mbsf) in two holes (U1592A and U1592B), terminating in limestone basement (all depths below seafloor [mbsf] are given using the core depth below seafloor, Method A [CSF-A], scale, except in **Operations** where the drilling depth below seafloor [DSF] scale is used). Average core recoveries were 71% (Hole U1592A) and 50% (Hole U1592B).

The Anafi Basin potentially recorded the full volcanic history of Santorini (and any older centers) since rift inception, but it was envisaged to probably also contain few eruptive products from

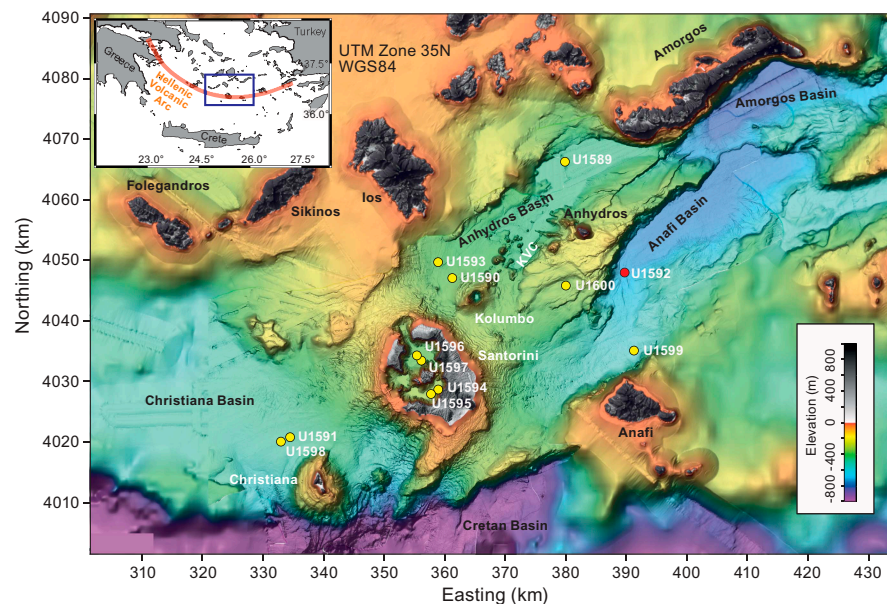


Figure F1. Site map. Red = Site U1592, yellow = other sites. Inset: location map. See Figure F1 in the Site U1589 chapter (Druitt et al., 2024) for citations for the swath data on which this map is based. KVC = Kolumbo volcanic chain.

Kolumbo. Drilling enabled reconstruction of the volcanic, sedimentary, and tectonic histories of the Anafi Basin, allowing us to compare its evolution with that of the Anhydros Basin. The site was also chosen to develop a core-log-seismic integration stratigraphy and compare it with the recently published seismic stratigraphy for the basin (Preine et al., 2022a, 2022b) and the paleotectonic reconstruction of the region (Nomikou et al., 2016, 2018). The site transects six seismic packages of the Anafi rift basin, as well as the onlap surfaces between them (Nomikou et al., 2016, 2018; Preine et al., 2022a) (Figure F2).

The Anafi Basin is crossed by many seismic profiles obtained in campaigns between 2006 and 2019, many of them multichannel (Hübscher et al., 2015; Nomikou et al., 2016, 2018). It is included within the area of the 2015 PROTEUS seismic tomography experiment, during which subbottom profiling, gravity, and magnetic data were also recorded (Hooft et al., 2017). The basin bathymetry had been studied in several marine campaigns, and fault distributions and throws had been mapped (Nomikou et al., 2016; Hooft et al., 2017). Previously published analyses of the seismic data suggested the following possible interpretations (from the bottom up; Preine et al., 2022a, 2022b):

- Units U1 and U2: sediment packages predating Santorini and Kolumbo volcanism;
- Unit U3: sediments and the products of the early Kolumbo volcanism and some of the Kolumbo cones;
- Unit U4: sediments associated with a major rift pulse; and
- Units U5 and U6: sediments and the products of Santorini activity, some of the Kolumbo cones, and the later eruptions of Kolumbo including the 1650 Common Era (CE) eruption.

Units U3–U6 were believed to be of Pleistocene age, and Units U1 and U2 were believed to be possibly Pliocene.

The site enabled us to test these interpretations by using the cores to reconstruct a near-complete volcanic stratigraphy consistent with both onshore and offshore constraints and pinned by chronological markers from biostratigraphy, magnetostratigraphy, and sapropel records. Benthic foraminifera from fine-grained sediments provided estimates of paleowater depths and, through integration with seismic profiles and chronologic data, of time-integrated basin subsidence rates.

Coring at Site U1592 in the Anafi Basin addressed scientific Objectives 1–4 and 6 of the Expedition 398 Scientific Prospectus (Druitt et al., 2022). It was complemented by Site U1589 in

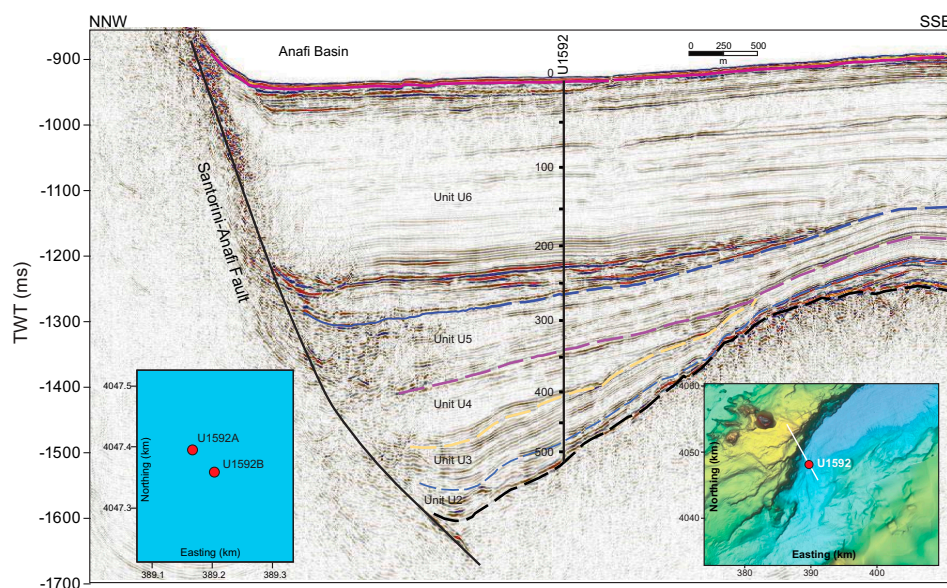


Figure F2. Seismic profile across the Anafi Basin along Seismic Line HH06-15. The basin fill has six seismic stratigraphic units (U1–U6), following Preine et al. (2022a). Insets: locations of Site U1592 and Holes U1592A and U1592B. Depths in meters. TWT = two-way traveltine.

the Anhydros Basin because each basin taps a different sediment distributary branch of the Christiana-Santorini-Kolumbo volcanic system.

2. Operations

Operations at Site U1592 involved two holes, with a switch to the rotary core barrel (RCB) system for Hole U1592B following slow progress with the extended core barrel (XCB) system. Hole U1592A was an advanced piston corer (APC), half-length APC (HLAPC), and XCB advance to 339.2 mbsf. Hole U1592B was RCB cored to 527.8 mbsf, with an initial 293.0 m drilled interval. Logging was not attempted because there were several sections of the same loose, unconsolidated layers that had caused problems at earlier sites.

2.1. Hole U1592A

On 14 January 2023, the rig crew proceeded to make up the APC/XCB bottom hole assembly (BHA) with a used bit. Hole U1592A was spudded at 0830 h from 700 meters below rig floor (mbrf) at 36°33.9358'N, 25°45.6784'E. The recovered core was 5.1 m, giving a calculated seafloor of 693.1 mbsl (Table T1). APC coring continued through Core 16H from 135.3 mbsf, but the last three cores suffered partial strokes. Coring was switched to the HLAPC system with Core 17F.

HLAPC coring continued on 15 January through Core 45F at 273.8 mbsf, where the barrel became stuck. Overpulls to 50,000 lb were ineffective. In attempting to drill over the barrel, the drill pipe became stuck, with indications the hole was filling in. The drill pipe was worked free, and eventually the barrel was freed with 120,000 lb overpull.

Table T1. Core summary, Site U1592. mbsf = meters below seafloor. NA = not applicable. DSF = drilling depth below seafloor. H = APC, F = HLAPC, X = XCB, numeric core type = drilled interval, R = RCB. (Continued on next page.) [Download table in CSV format.](#)

Hole U1592A		Hole U1592B	
Latitude: 36°33.9358'N		Latitude: 36°33.9164'N	
Longitude: 25°45.6784'E		Longitude: 25°45.7027'E	
Water depth (m): 693.11		Water depth (m): 693.11	
Date started (UTC): 0215 h; 14 January 2023		Date started (UTC): 0915 h; 16 January 2023	
Date finished (UTC): 0915 h; 16 January 2023		Date finished (UTC): 1900 h; 18 January 2023	
Time on hole (days): 2.29		Time on hole (days): 2.41	
Penetration (mbsf): 339.2		Penetration (mbsf): 527.8	
Cored interval (m): 339.2		Cored interval (m): 234.8	
Recovered length (m): 240.45		Recovered length (m): 117.04	
Recovery (%): 70.89		Recovery (%): 49.85	
Drilled interval (m): NA		Drilled interval (m): 293	
Drilled interval (no.): 0		Drilled interval (no.): 1	
Total cores (no.): 55		Total cores (no.): 25	
APC cores (no.): 16		RCB cores (no.): 25	
HLAPC cores (no.): 29			
XCB cored (no.): 0			

Core	Top depth drilled DSF (m)	Bottom depth drilled DSF (m)	Interval advanced (m)	Recovered length (m)	Core recovery (%)	Core on deck date (2023)	Core on deck time UTC (h)
398-U1592A-							
1H	0.0	5.1	5.1	5.10	100	14 Jan	0640
2H	5.1	14.6	9.5	9.44	99	14 Jan	0725
3H	14.6	24.1	9.5	9.91	104	14 Jan	0800
4H	24.1	33.6	9.5	9.44	99	14 Jan	0825
5H	33.6	43.1	9.5	9.93	105	14 Jan	0855
6H	43.1	52.6	9.5	9.83	103	14 Jan	0915
7H	52.6	62.1	9.5	10.04	106	14 Jan	0940
8H	62.1	71.6	9.5	10.01	105	14 Jan	1005
9H	71.6	81.1	9.5	9.92	104	14 Jan	1035
10H	81.1	90.6	9.5	9.58	101	14 Jan	1100
11H	90.6	100.1	9.5	9.34	98	14 Jan	1130
12H	100.1	109.6	9.5	9.08	96	14 Jan	1200
13H	109.6	117.5	7.9	7.95	101	14 Jan	1230
14H	117.5	125.8	8.3	8.31	100	14 Jan	1305

Table T1 (continued).

Core	Top depth drilled DSF (m)	Bottom depth drilled DSF (m)	Interval advanced (m)	Recovered length (m)	Core recovery (%)	Core on deck date (2023)	Core on deck time UTC (h)
15H	125.8	135.3	9.5	0.00	0	14 Jan	1340
16H	135.3	137.5	2.2	2.22	101	14 Jan	1440
17F	137.5	142.2	4.7	4.27	91	14 Jan	1610
18F	142.2	146.9	4.7	3.51	75	14 Jan	1645
19F	146.9	151.6	4.7	1.25	27	14 Jan	1715
20F	151.6	156.3	4.7	4.26	91	14 Jan	1750
21F	156.3	161.0	4.7	1.95	41	14 Jan	1835
22F	161.0	165.7	4.7	2.90	62	14 Jan	1910
23F	165.7	170.4	4.7	0.51	11	14 Jan	1940
24F	170.4	175.1	4.7	3.10	66	14 Jan	2010
25F	175.1	179.8	4.7	4.66	99	14 Jan	2130
26F	179.8	184.5	4.7	3.36	71	14 Jan	2155
27F	184.5	189.2	4.7	2.87	61	14 Jan	2225
28F	189.2	193.9	4.7	3.89	83	14 Jan	2255
29F	193.9	198.6	4.7	3.24	69	14 Jan	2320
30F	198.6	203.3	4.7	1.89	40	14 Jan	2345
31F	203.3	208.0	4.7	0.10	2	15 Jan	0020
32F	208.0	212.7	4.7	2.49	53	15 Jan	0110
33F	212.7	217.4	4.7	0.13	3	15 Jan	1035
34F	217.4	222.1	4.7	3.15	67	15 Jan	0200
35F	222.1	226.8	4.7	2.28	49	15 Jan	0245
36F	226.8	231.5	4.7	2.03	43	15 Jan	0315
37F	231.5	236.2	4.7	2.27	48	15 Jan	0340
38F	236.2	240.9	4.7	1.60	34	15 Jan	0405
39F	240.9	245.6	4.7	2.82	60	15 Jan	0430
40F	245.6	250.3	4.7	0.99	21	15 Jan	0520
41F	250.3	255.0	4.7	1.33	28	15 Jan	0610
42F	255.0	259.7	4.7	2.10	45	15 Jan	0640
43F	259.7	264.4	4.7	2.40	51	15 Jan	0725
44F	264.4	269.1	4.7	1.47	31	15 Jan	0750
45F	269.1	273.8	4.7	3.52	75	15 Jan	1010
46X	273.8	278.0	4.2	2.52	60	15 Jan	1245
47X	278.0	287.7	9.7	9.48	98	15 Jan	1440
48X	287.7	297.4	9.7	4.99	51	15 Jan	1630
49X	297.4	307.1	9.7	8.58	88	15 Jan	1850
50X	307.1	316.8	9.7	2.73	28	15 Jan	2110
51X	316.8	326.5	9.7	1.34	14	15 Jan	2335
52X	326.5	331.0	4.5	3.01	67	16 Jan	0110
53X	331.0	336.2	5.2	5.81	112	16 Jan	0240
54X	336.2	337.2	1.0	0.37	37	16 Jan	0405
55X	337.2	339.2	2.0	1.18	59	16 Jan	0510
398-U1592B-							
11	0.0	293.0	293.0	****Drilled interval****		16 Jan	2300
2R	293.0	302.7	9.7	6.32	65	17 Jan	0035
3R	302.7	312.4	9.7	8.51	88	17 Jan	0210
4R	312.4	322.1	9.7	3.45	36	17 Jan	0310
5R	322.1	331.8	9.7	7.34	76	17 Jan	0430
6R	331.8	341.5	9.7	8.23	85	17 Jan	0550
7R	341.5	351.2	9.7	6.54	67	17 Jan	0705
8R	351.2	360.9	9.7	0.00	0	17 Jan	0750
9R	360.9	370.6	9.7	0.00	0	17 Jan	0920
10R	370.6	380.3	9.7	0.01	0	17 Jan	1030
11R	380.3	382.3	2.0	0.01	1	17 Jan	1150
12R	382.3	392.0	9.7	0.00	0	17 Jan	1320
13R	392.0	401.7	9.7	0.00	0	17 Jan	1420
14R	401.7	411.4	9.7	3.26	34	17 Jan	1550
15R	411.4	421.1	9.7	5.26	54	17 Jan	1725
16R	421.1	430.8	9.7	7.41	76	17 Jan	1905
17R	430.8	440.5	9.7	9.11	94	17 Jan	2045
18R	440.5	450.2	9.7	8.69	90	17 Jan	2225
19R	450.2	459.9	9.7	6.91	71	18 Jan	0010
20R	459.9	469.6	9.7	9.74	100	18 Jan	1045
21R	469.6	479.3	9.7	7.91	82	18 Jan	0300
22R	479.3	489.0	9.7	6.46	67	18 Jan	0420
23R	489.0	498.7	9.7	4.61	48	18 Jan	0535
24R	498.7	508.4	9.7	4.20	43	18 Jan	0755
25R	508.4	518.1	9.7	1.39	14	18 Jan	1025
26R	518.1	527.8	9.7	1.68	17	18 Jan	1330
Totals:			867.0	357.49			

Once free, the HLAPC barrel and sinker bars were pulled. A single drill pipe joint was pulled so the hole could be reconditioned. The driller pumped mud sweeps while working the drill string. Once the hole had improved, the HLAPC hole was drilled out.

At 1330 h, an XCB barrel was dropped and coring reconvened with Core 46X from 273.8 mbsf. Coring continued on 16 January through Core 55X at 339.2 mbsf, the final depth for Hole U1592A. The rate of penetration for the XCB system was slowing to the 4 m/h range, so the decision was made to switch to the RCB system.

There were damaged and missing cutters on the XCB cutting shoes. Although the formation resulted in good recovery, it seemed to be too hard on the shoes.

At 0730 h on 16 January, XCB coring was terminated. The drill string was tripped out with the top drive from 339.2 to 285.5 mbsf. The top drive was racked back, and the pipe trip continued. The bit cleared the seafloor at 0915 h. The bit cleared the rotary table at 1120 h, ending Hole U1592A.

The rate of penetration for the XCB system averaged 7.9 m/h but dropped to ~4 m/h over the last two to three cores.

2.2. Hole U1592B

On 16 January 2023 at 1120 h, the crew began making up the RCB BHA with bit. Following this, the rig was serviced. The BHA was then run in to 688 mbrf, where the top drive was picked up. The drill string was spaced out, and a center bit was deployed. Meanwhile, the vessel was offset 50 m southeast of Hole U1592A.

Hole U1592B was spudded at 1600 h at 36°33.9164'N, 25°45.7027'E. The seafloor depth was again 693.1 mbsl by offset. Drill-ahead commenced and advanced to 286.8 mbsf by midnight. Liberal mud sweeps were used to keep the hole clean. Drill-down finished at 0100 h on 17 January at 293.0 mbsf. The center bit was recovered, and an RCB barrel was dropped.

The driller started RCB coring with Core 2R from 293.0 mbsf. Cores 8R–13R were almost zero recovery and were assumed to be a pumice layer, judging from the seismic profiles. Core 11R was a punch core, a 2 m advance with little to no rotation or pump, to try to recover some of the difficult pumice section. The recovery was still very poor but measurable because it recovered a handful of the ground pumice. Following Core 12R, the drill string became stuck, requiring several minutes, 100,000 lb of overpull, and two mud sweeps to come free.

Coring continued on 18 January until 1545 h with Core 26R to 527.8 mbsf, the final depth for Hole U1592B. The drill string was tripped up with the top drive from 527.8 to 448.9 mbsf. The top drive was racked back, and the pipe trip recommenced, clearing the seafloor at 1748 h, with the bit clearing the rotary table at 2001 h. The rig crew secured the floor for transit.

The thrusters were raised beginning at 2048 h. The vessel was out of dynamic positioning control at 2052 h. All thrusters were up and secure, and the sea passage started at 2100 h, ending Site U1592.

The rate of penetration for the RCB system averaged 16.0 m/h (not including wireline time).

3. Lithostratigraphy

Cores from Site U1592 recovered a fairly coherent stratigraphy from 0 to 519.77 mbsf (Figure F3). Hole U1592A consists of Cores 1H–55X (0–338.35 mbsf). Hole U1592B consists of Sections 2R-1 through 26R-1 (293.0–518.92 mbsf). The goal for Hole U1592B was to overlap coring depth with the bottom of Hole U1592A using the RCB system for better recovery and then continuing to deeper levels. Lithostratigraphic Unit I is unlithified sediment dominated by volcanic and tuffaceous material in the uppermost 266 m, with lesser nonvolcanic lithologies. This unit transitions downward to Unit II, which consists dominantly of ooze and other nonvolcanic lithologies interspersed with minor volcanic and tuffaceous sediments to 403.93 mbsf. Unit III is ~90 m thick and comprises dolomitic mud and sand with shell fragments that transitions downward into Unit IV, a

thin (~15 m) unit of bioclastic limestone. Unit V is ~10 m of limestone and marble defined as basement.

In Unit I, the succession of volcanic layers and tuffaceous or nonvolcanic layers defines four subunits (Ia–Id). These subunit distinctions are corroborated by physical property data (i.e., magnetic susceptibility [MS] and natural gamma radiation [NGR]; see **Physical properties**). Smear slides for microscopic analyses were prepared to confirm macroscopic descriptions of distinct lithology changes at the section level, such as identification of vitric ash particles in tuffaceous lithologies or crystals in ash layers. Units II–V do not exhibit sufficient variation to warrant subunits.

Figure F3 summarizes the lithostratigraphy of Site U1592, displaying recovery and lithostratigraphic units and subunits in Holes U1592A and U1592B. Table T2 provides the upper and lower boundaries, thicknesses, biostratigraphic ages (see **Biostratigraphy**), and lithologic summaries of the units and subunits. Figure F4 graphically presents the relative proportions of volcanic, tuffaceous, and nonvolcanic lithologies in each hole. Figure F5 presents grain size distributions of the sediments in all units, particularly the changes in grain size within the volcanic- and tuffaceous-dominated units, to graphically show the distribution of ash, lapilli-ash, and lapilli. Figure F6 displays different types of core disturbance observed at Site U1592.

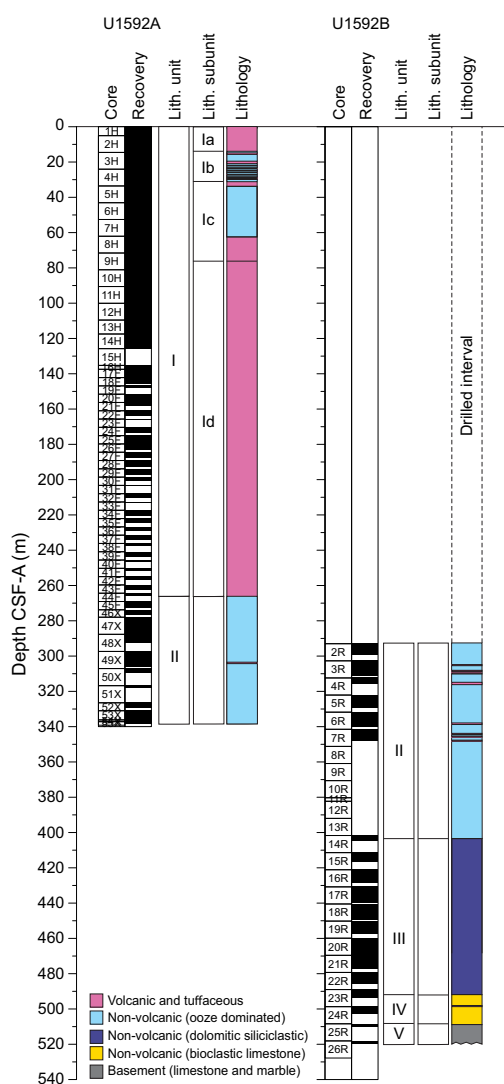


Figure F3. Lithostratigraphic summary, Site U1592. Lithostratigraphic Unit I is divided into four subunits that are further characterized in Figures F4 and F5. Unit color = dominant lithology.

Table T2. Lithostratigraphic units and subunits, Site U1592. * = bottom not recovered. † = end of hole. [Download table in CSV format.](#)

Lith. unit	Subunit	Top depth (mbsf)	Top hole, core, section, interval (cm)	Bottom depth (mbsf)	Bottom hole, core, section, interval (cm)	Thickness (m)	Lithologic summary
I	la	0.00	U1592A-1H-1, 0	13.19	U1592A-2H-6, 57	13.19	Lapilli-dominated with minor ash and lapilli-ash
	lb	13.19	U1592A-2H-6, 57	30.84	U1592A-4H-5, 74	17.65	Ooze-dominated, ooze with minor ash, ooze with ash, tuffaceous ooze, and organic-rich mud
	lc	30.84	U1592A-4H-5, 74	76.64	U1592A-9H-4A, 57	45.80	Very fine-grained (clay/fine ash), ash, then ooze grading downhole to ooze with ash to tuffaceous ooze
	ld	76.64	U1592A-9H-4, 57	269.10	U1592A-44F-CC, 19	192.46	Ash-dominated with minor ash with lapilli and lithic lapilli
II		269.10	U1592A-45F-1, 0	338.35	U1592A-55X-CC, 7*†	~135	Ooze-dominated with shell fragments
		—	—	403.93	U1592B-14R-2, 74	~135	Ooze-dominated with shell fragments
III		403.93	U1592B-14R-2, 74	493.48	U1592B-23R-CC, 10	89.55	Dolomitic siliciclastic with shells
IV		493.50	U1592B-23R-CC, 12	508.75	U1592B-25R-1, 35	15.25	Bioclastic limestone
V		508.75	U1592B-25R-1, 35	519.77	U1592B-26R-2, 85*†	>11.02	Basement (limestone and marble)

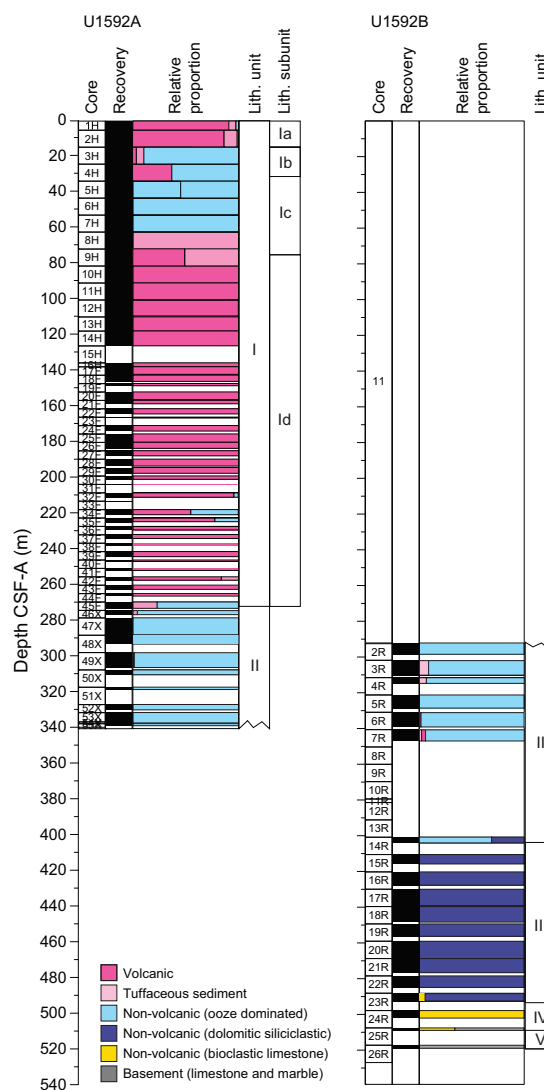


Figure F4. Relative percentages of volcanic, tuffaceous, and nonvolcanic lithologies, Site U1592. Unit I is volcanic dominated compared to Units II–V.

The following sections describe (1) the effects of core disturbance, (2) the five lithostratigraphic units and subunits, (3) correlations between Holes U1592A and U1592B, and (4) X-ray diffraction (XRD) results from Site U1592.

3.1. Core disturbance

Several types of core disturbance disrupt the lithostratigraphy at Site U1592 (Figure F6):

- Uparching: slight to moderate coring-induced shear between the sediment and core liner results in bedding uniformly dragged downward along the core margins (Figure F6A). In these intervals, the original lithofacies and sedimentary structures are usually slightly to severely disturbed but can still be recognized visually.
- Fall-in: coarse clast-supported or, in some cases, finer grained muddy intervals at the tops of many cores (Figure F6B). In these intervals, which may reach up to 23 cm in thickness, original lithofacies and sedimentary structures are not present.
- Biscuiting: fractured disc-shaped pieces, ranging in size from a few centimeters to more than 10 cm, often packed with sheared and remolded core material mixed with drill slurry, filling gaps between brittle biscuits (Figure F6C). The degree of biscuiting ranges from slight to

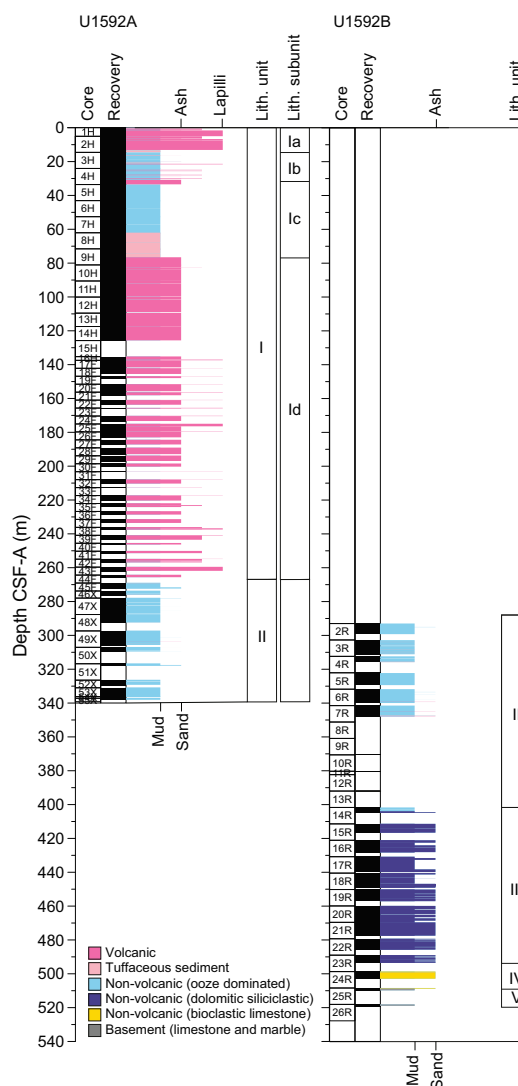


Figure F5. Grain size distribution of volcanic, tuffaceous, and nonvolcanic sediments, Site U1592. Length of colored bars = relative grain size (ash = <2 mm; lapilli = 2–64 mm; mud = <63 μ m; sand = 0.063–2 mm), with separate scales shown for volcanic grain size (top) and tuffaceous and nonvolcanic grain size (bottom). Mixed lithologies such as lapilli-ash (dark pink) that have relative grain sizes between two categories are plotted between ticks.

severe, depending on the size of the biscuits and the proportion of biscuits to infill material. Biscuiting is frequently observed in cores recovered by RCB and XRB coring.

- Brecciated: core extension disturbs the core until it becomes sheared, or, in the case of brittle failure, brecciated (Figure F6D). Slight brecciation produces cracks in the original lithologies (Figure F6E), whereas moderate to severe brecciation disturbs original lithofacies and sedimentary structures more severely, although they usually remain readily recognizable. In contrast, the contacts between intervals and stratifications in granular layers may be lost due to brecciation.
- Sediment flowage: softer or less cohesive units are plastically mixed with harder, more cohesive units either during shaking or biscuiting or due to underpressure of a partial stroke and flows along the core liner, sometimes subsequently deposited in cracks of more consolidated sediments. Relics of squeezed sediment are visible between the liner and the sediment (Figure F6F).
- Artificial size and density segregation: occurs during drilling or with postrecovery core handling processes on board (e.g., inclining, shaking, and plunging cores on the catwalk to compact sediments). Jutzeler et al. (2014) also described pseudohorizontal density grading that can occur while the core is lying flat on deck, resulting in vertical structures once the core is turned upright. Such core disturbance is observed most often in volcanic sediments because increased porosity allows sucking in of seawater during hydraulic piston coring. The resulting soupy texture allows material to flow within the core liner. Secondary normal or reverse grading, or density separation of clasts, may occur as a result of this disturbance and obscure primary sedimentary features.

3.2. Description of units and subunits

The sediments recovered from Holes U1592A and U1592B comprise five lithostratigraphic units (I–V) (Figure F3). Unit I is divided into four subunits (Ia–Id). (Figures F4, F5; Table T2). The lithology of these units and subunits is described below.

3.2.1. Unit I

Interval: 398-U1592A-1H-1, 0 cm, to 44F-CC, 19 cm

Thickness: 269.1 m

Depth: 0.00–269.1 mbsf

Age: Holocene to Middle Pleistocene

Lithology: volcanic and tuffaceous lithologies (ash, lapilli, and lapilli-ash and tuffaceous mud/ooze) and minor ooze, organic-rich ooze/mud, and ooze with ash/lapilli

Unit I was only recovered in Hole U1592A. It extends from 0 to 269.1 mbsf (Table T2) and consists of mainly pumice lapilli in the uppermost 13 m (Subunit Ia); a repetitive sequence of nonvolcanic

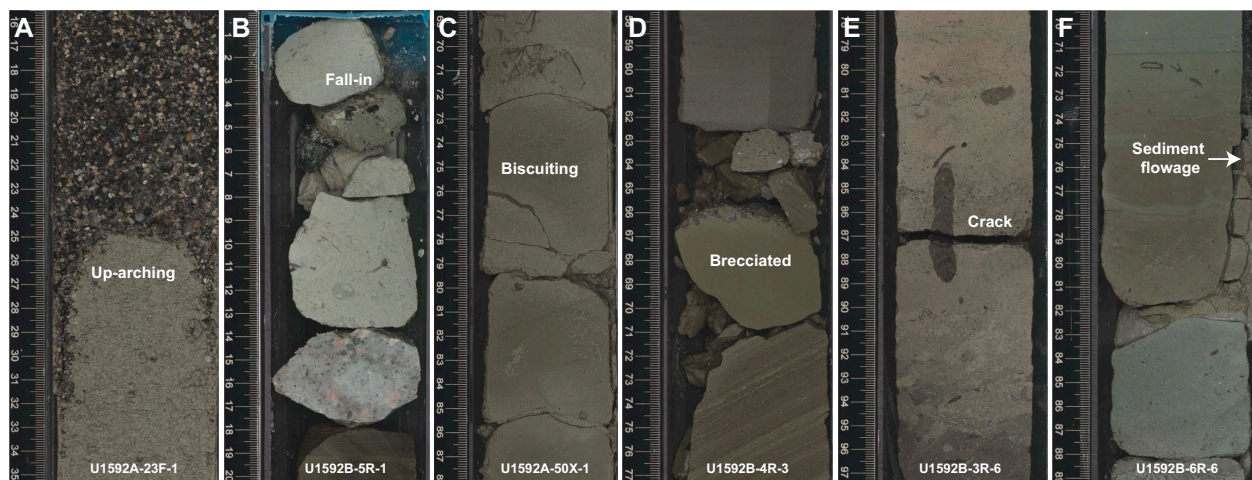


Figure F6. Core disturbances, Site U1592. A. Uparching. B. Fall-in. C. Biscuiting. D. Brecciation. E. Crack. F. Sediment flowage.

and volcanic sediments for ~18 m (Subunit Ib); a nonvolcanic-dominated, very fine-grained sequence with volcanic sediments at its top and base (Subunit 1c); and an extensive 189 m thick ash interval at the base of the unit (Subunit Id) (Figures F4, F5). Volcanic intervals commonly have sharp bottom contacts with tuffaceous or nonvolcanic lithologies. Figure F7 highlights core images of the most common lithologies collected from Unit I. Figure F8 shows representative smear slides from these lithologies.

Volcanic lithologies (>75% volcanic particles; glass shards, pumice, and crystals) comprise ash, lapilli-ash, and lapilli. Description of these lithologies in volcanic intervals was based on the relative abundance of ash-sized (<2 mm) and lapilli-sized (2–64 mm) particles, as described in **Lithostratigraphy** in the Expedition 398 methods chapter (Kutterolf et al., 2024), with ash and lapilli

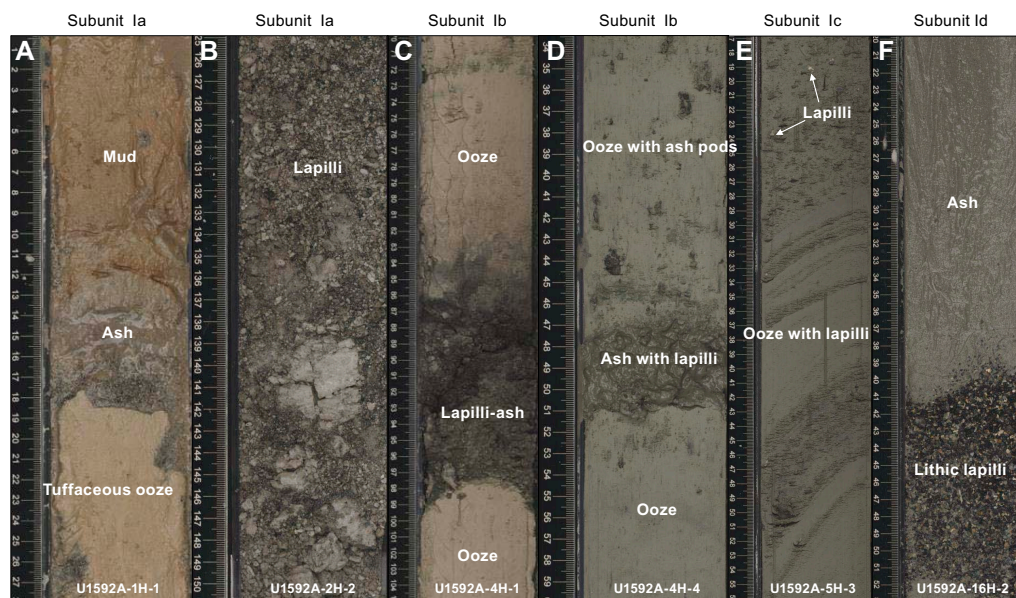


Figure F7. A–E. Common lithologies from Unit I, Hole U1592A. Unit I is dominated by volcanic and tuffaceous lithologies, but Subunits Ib and Ic have a higher proportion of ooze.

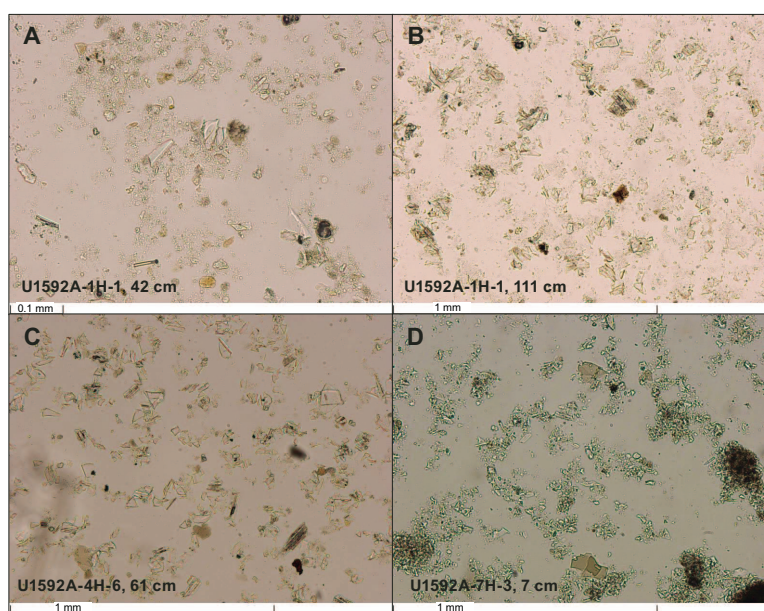


Figure F8. Representative lithologies from Unit I, Hole U1592A. A. Tuffaceous ooze. B, C. Ash layers. D. Ooze with ash interval.

used when the proportion of one size was >75% and lapilli-ash described when both sizes were present but at <75% abundance (Fisher and Schmincke, 1984).

Macroscopically, ash layers in Site U1592 Unit I are typically gray, well sorted, range from fine to coarse ash, and are variably admixed with nonvolcanic sediment at the upper contact. They are easily identified in Unit I by their hydrophilic nature in contrast to drier overlying tuffaceous muds/oozes (Figure F9). Thicknesses of layers in Unit I are highly variable from centimeter to meter scale (e.g., a 2 cm thick ash layer in Section 398-U1592A-3H-2 and a 189 m thick ash interval that marks the base of Unit I). Layers are frequently characterized by a sharp base and a more diffuse and often bioturbated upper boundary that grades into tuffaceous mud or ooze. Microscopic observations of smear slides were useful for identification of specific minerals, especially biotite.

Lapilli and lapilli-ash layers are typically dark gray to dark brownish gray (Figure F7) and range from a few centimeters to several meters thick. They are often truncated at the lower boundary by loss of recovery, so recovered contacts with underlying material are rare. Where recovered, lower contacts of these coarser units are sharp or bioturbated but commonly affected by uparching drilling disturbance.

Subunits in Unit I were defined by the relative proportion of volcanic/tuffaceous intervals and nonvolcanic intervals, as well as by grain size:

- Subunit Ia (Sections 398-U1592A-1H-1, 0 cm, through 2H-6, 57 cm; 0–13.19 mbsf): primarily lapilli, with minor ash and lapilli-ash.
- Subunit Ib (Sections 2H-6, 57 cm, through 4H-5, 74 cm; 13.19–30.84 mbsf): primarily nonvolcanic material consisting of ooze, ooze with ash/lapilli, organic-rich ooze/mud, with minor intervals of tuffaceous ooze, ash, lapilli-ash, and lapilli.
- Subunit Ic (Sections 4H-5, 74 cm, through 9H-4, 57 cm; 30.84–76.64 mbsf): primarily clay-sized nonvolcanic sediments (ooze/mud) capped by ash at the upper boundary and volcanic sediments (ash, lapilli, and tuffaceous sediments) at the lower boundary.
- Subunit Id (Sections 9H-4, 57 cm, through 44F-CC, 19 cm; 76.64–269.1 mbsf): primarily ash with intervals of lithic-rich lapilli.

3.2.1.1. Subunit Ia

Subunit Ia extends for 13.19 m in Hole U1592A (Sections 1H-1, 0 cm, through 2H-6, 57 cm) (Figure F3; Table T2) and consists primarily of volcanic lithologies with small amounts of mud and tuffaceous mud (47 cm of 13.19 m). The subunit begins with 10 cm of mud underlain by a 6 cm thick biotite-bearing ash, in turn underlain by a 30 cm thick pale brown tuffaceous mud (Figure F7A). The rest of the subunit is volcanic, dominated by well-sorted coarse ash to medium lapilli

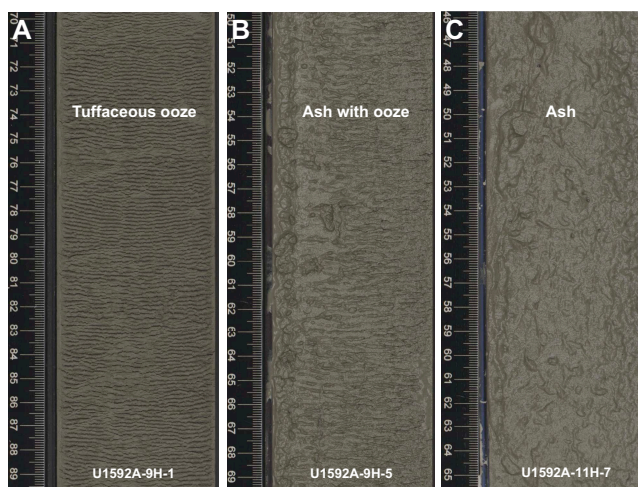


Figure F9. A–C. Transition from tuffaceous ooze to ash, Hole U1592A. This transition in (A) wet to (C) dry appearance consistently marks the increasing admixture of sediment with ash upward.

(Figure **F7B**) with dark/reddish lithics and crystals at the base of each core. Clasts are millimeter- to centimeter-sized white and gray pumice. Pumice and lithic clasts are subangular to subrounded. This subunit is characterized by low average grain density, high MS, and moderate NGR (see **Physical properties**).

3.2.1.2. Subunit Ib

Subunit Ib is a heterogeneous unit that is dominated by ooze but has some repetitive nonvolcanic and volcanic intervals. The top of the subunit is the first ooze interval that underlies the last lapilli interval of Subunit Ia; it is marked by an abrupt increase in bulk/grain density (see **Physical properties**). The subunit is 17.65 m thick and extends from 13.19 to 30.84 mbsf in Hole U1592A (Sections 2H-6, 57 cm, through 4H-5, 74 cm) (Figure **F3**; Table **T2**). The subunit continues downward into grayish brown to greenish gray oozes with variable componentry ranging from pure ooze to ooze with lapilli or ash, tuffaceous ooze with or without lapilli, and organic-rich ooze/mud. These oozes are punctuated by several centimeter- to decimeter-thick ashes and lapilli ashes (dark gray to black) that stand out in contrast to the oozes above and below (Figure **F7C**, **F7D**). These ash layers are characterized by jumps in MS (see **Physical properties**). Some of the oozes contain ash pods and shell fragments.

3.2.1.3. Subunit Ic

Subunit Ic extends from 30.84 to 45.8 mbsf in Hole U1592A (Sections 4H-5, 74 cm, through 9H-4, 57 cm) (Figure **F3**; Table **T2**). This subunit is dominated by clay-sized particles and begins with an ash layer that transitions downward into a unique clay-sized ooze, ooze with ash, and tuffaceous ooze. These intervals have distinctly high NGR and low MS (see **Physical properties**). Some shell fragments and pumice lapilli are observed in the upper part of the subunit. Section 5H-3 is characterized by the presence of a large slump (Figure **F7E**). Subunit Ic ends with a thick tuffaceous ooze interval.

3.2.1.4. Subunit Id

Subunit Id was recovered from 76.64 to 265.85 mbsf in Hole U1592A (Sections 9H-4A, 57 cm, through 44F-CC, 19 cm) (Figure **F3**; Table **T2**). The total thickness of this subunit is 192.46 m, and it is dominated by one very thick ash layer with occasional lithic lapilli that occur either as fall-in or as discrete layers within ash. The ash is biotite bearing and typically well sorted with occasional lapilli-ash or ash with lapilli. The uppermost 100 m of the ash is dominantly fine ash, transitioning to coarse ash below and then to lapilli-ash and lapilli in the lowermost 40 m.

Lithic lapilli intervals are polymictic and contain dark volcanic rocks, subrounded pumice, plagioclase, and shell fragments. Below Core 398-U1592A-16H, the lithic lapilli are generally at the top of cores (i.e., fall-in). Discrete layers of (non-fall-in) lithic lapilli are observed in Sections 16F-2 (Figure **F7F**), 21F-1, 43F-1, and 35F-2.

Two <10 cm brown mud intervals are observed at the tops of Cores 20F and 27F. This may be fall-in or may represent quiescent intervals before further deposition of ash. These muds are poorly sorted and contain volcanic rock lithics, scoria, and subrounded pumice.

3.2.2. Unit II

Intervals: 398-U1592A-45F, 0 cm, to 55X-CC, 7 cm (bottom of hole); 398-U1592B-2R-1, 0 cm, to 14R-2, 74 cm

Thickness: ~112.83 m

Depths: Hole U1592A = 269.1–338.35 mbsf; Hole U1592B = 293–403.92 mbsf

Age: Middle Pleistocene to Early Pleistocene (see **Biostratigraphy**)

Lithology: nonvolcanic, ooze-dominated lithologies (ooze, organic-rich ooze, ooze with ash/lapilli, mud, and tuffaceous mud) with lesser ash and sand

Unit II (Figure **F3**; Table **T2**) was recovered from 269.1 to 338.35 mbsf in Hole U1592A and from 293 to 403.92 mbsf in Hole U1592B. It primarily comprises ooze-dominated lithologies interspersed with minor intervals of organic-rich ooze, mud, tuffaceous mud, ash, and sand (Figure **F10**). In Hole U1592A, Unit II is marked by a distinctive shift in lithology from volcanic to nonvolcanic and ooze-dominated, corroborated by a jump to higher grain density (see **Physical**

properties). Coring in Hole U1592B bypassed all of Unit I, and the first cores are lithologically similar to those of Unit II in Hole U1592A. Unit II terminates at the first appearance of dolomitic ooze and sand.

Oozes generally appear gray to greenish gray and variably contain lapilli, shells, and lithics. Intervals of organic-rich (sapropelic) ooze occur throughout Unit II, often identified by a gradational change from greenish gray ooze to dark brownish gray ooze. These organic-rich intervals are generally 20–30 cm thick and often display a higher degree of bioturbation than surrounding material. Intervals of ooze containing 1%–25% volcanic material (with lapilli, lithics, or ash pods) occur commonly at the top of Unit II (Cores 398-U1592A-45X through 50X) and in the middle (Cores 398-U1592B-2R through 6R). Scoria lapilli are especially common in Cores 2R–4R.

Smear slides taken in Unit II allowed for identification of biogenic components (e.g., proportion of nannofossils) and confirmation of tuffaceous lithologies that could not be macroscopically determined. Sedimentary lithics, calcite, foraminifera, sponge spicules, pyrite, and feldspar were often observed in microscopic smear slide descriptions (Figure F11).

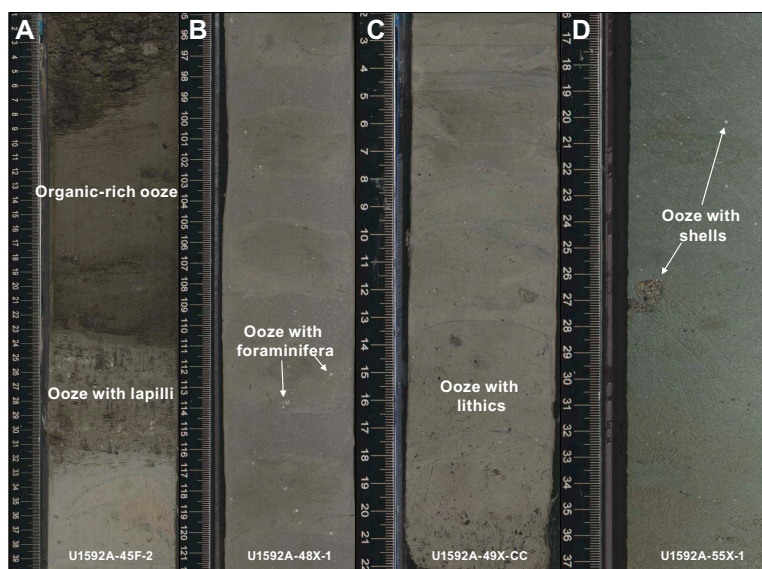


Figure F10. Common lithologies from Unit II, Hole U1592A. Dominant nonvolcanic sediments (ooze) generally appear gray to greenish gray and may contain (A) lapilli, (B) foraminifera, (C) lithics, and (D) shells. Intervals of organic-rich ooze are observed throughout Unit II, often identified by a gradational change from greenish gray ooze to dark brownish gray ooze.

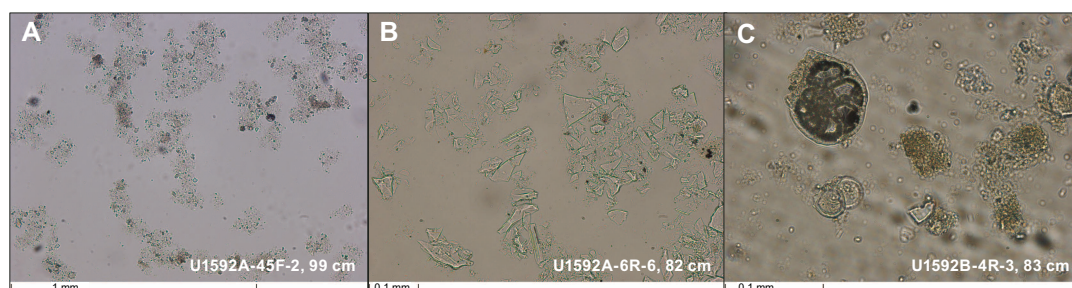


Figure F11. Representative lithologies from Unit II, Site U1592. A. Nannofossil ooze with calcite, pyrite, and sponge spicules. B. Ash consisting of transparent cusped and pumiceous vitric grains. C. Microfossils such as benthic and planktonic foraminifera.

3.2.3. Unit III

Interval: 398-U1592B-14R-2A, 74 cm, to 23R-CC, 10 cm

Thickness: 89.55 m

Depth: 403.93–493.48 mbsf

Age: Early Pleistocene (see [Biostratigraphy](#))

Lithology: dolomitic sand with periodic intervals of dolomitic mud with organic material

Unit III was only recovered in Hole U1592B and extends from 403.93 to 493.48 mbsf (Sections 14R-2, 74 cm, through 23R-CC, 10 cm) (Figures [F3](#), [F4](#); Table [T2](#)). The total thickness of this sub-unit is 89.55 m. The upper boundary is defined by the first appearance of dolomitic ooze and sand with shell fragments. The unit consists of greenish gray dolomitic sand with periodic intervals of organic-rich dolomitic mud. The dolomitic character was defined by XRD and using 20% HCl, which reacted strongly with the rock compared to 10% HCl (see [X-ray diffraction](#)) (Figure [F12](#)). The fine-grained and well-sorted dolomitic sands are characterized by the presence of biogenic clasts including shell fragments, foraminifera, and plant fragments (Section 17R-3, 131 cm) (Figure [F13A–F13D](#)). Disseminated sulfides are present throughout the unit, but nodules of pyrite are sparsely dispersed. Some fine to medium lapilli of pumice and scoria are observed in Sections 21R-1 and 21R-4 (Figure [F13E](#)). Dolomitic sand intervals are only slightly bioturbated, whereas organic-rich intervals are more highly bioturbated and display numerous well-preserved traces of *Chondrites* and *Zoophycos* (Figure [F13F](#)). These organic-rich intervals are commonly thinly laminated (<0.3 cm thick) and display a gradational upper contact and a horizontal sharp lower contact. The lower contact of the unit is observed in Section 23R-CC, where it terminates abruptly against the bioclastic limestone of Unit IV.

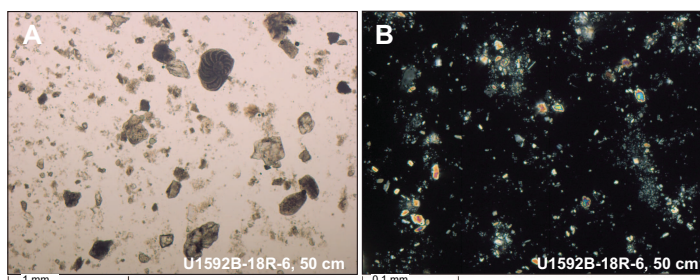


Figure F12. Dolomitic ooze observed in Unit III, Hole U1592B. A. Foraminifera. B. Dolomite.

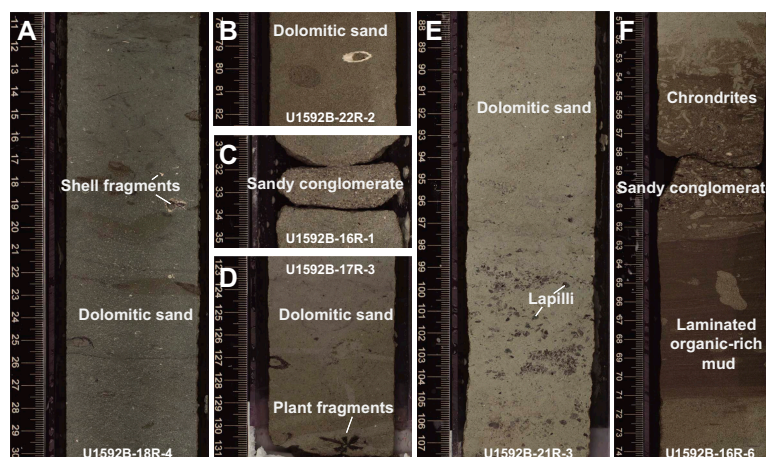


Figure F13. Common lithologies from Unit III, Hole U1592B. A–E. Dominant dolomitic sand containing (A–C) shell fragments, (D) plant fragments, and (E) lapilli. F. Periodic organic-rich intervals are more highly bioturbated and display numerous well-preserved traces of *Chondrites* and *Zoophycos*.

3.2.4. Unit IV

Interval: 398-U1592B-23R-CC, 12 cm, to 25R-1, 35 cm

Thickness: 15.25 m

Depth: 493.5–508.75 mbsf

Age: likely Early Pleistocene (see [Biostratigraphy](#))

Lithology: bioclastic limestone

Unit IV, observed in Hole U1592B only, consists of bioclastic limestone, with two 1–2 cm thick interbedded bioclastic tuff intervals in Section 24R-1. The recovered lithologies extend from 493.5 to 508.75 mbsf, reaching a thickness of 15.25 m (Table [T2](#)).

The top of this unit occurs as an abrupt transition in Section 398-U1592B-23R-CC from the greenish dolomitic sand of Unit III to bioclastic limestone. This transition is marked by a significant increase in *P*-wave velocity and density, lower NGR, and higher thermal conductivity compared with the overlying units (see [Physical properties](#)).

The bioclastic limestone is white to pale yellow, poorly sorted, and matrix- to clast-supported (Figure [F14](#)). The matrix is typically light gray and calcareous with either micritic or sparry calcite present. Clasts (>2 mm) are mainly biogenic and are predominantly foraminifera, bivalves, gastropods, corals, and coralline red algae, among other bioclasts. Clasts of volcanic, sedimentary (e.g., sandstone), and metamorphic rock were also observed. Dark-colored (volcanic) clasts increase in abundance and size toward the bottom of Section 24R-2 and disappear toward the bottom of Section 24R-3. The bioclastic limestone present in Unit IV bears similarities to the carbonate-cemented, oxidized siliciclastics found in Unit IV at Site U1589, although they are not as heavily altered.

Two bioclastic tuff intervals are intercalated within the bioclastic limestone (intervals 24R-1, 27–28 and 47–49 cm). The tuffs are light greenish gray and moderately sorted. They consist of coarse ash and clasts of metamorphic rock as well as shell fragments. No grading or bioturbation was observed in these layers, and there are no occurrences of organic-rich (sapropelic) lithologies.

Figure [F15A–F15D](#) shows selected thin section images of bioclastic limestone of this unit. The bioclastic limestones are matrix- to clast-supported and contain component (allochemical) parti-

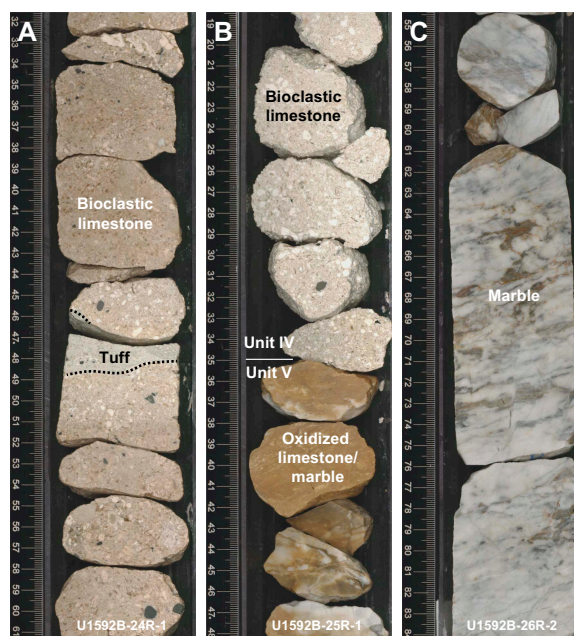


Figure F14. Lithologies from Units IV and V, Hole U1592B. A. Bioclastic limestone of Unit IV with two 1–2 cm thick interbedded bioclastic tuff intervals. B. Unit IV/V boundary. C. Oxidized limestone and marble cobbles of Unit V.

cles of predominantly bioclasts including benthic and planktonic foraminifera, bivalves, gastropods, corals, and coralline red algae. Minor lithic components including sedimentary and metamorphic rock types were also observed in some of the thin sections. Matrices are either micritic or consist of sparry calcite cement. The bioclastic limestones of Unit IV are classified as packed biomicrite or unsorted biosparite according to the classification scheme of Folk (1959) or as packstone or grainstone in the limestone classification scheme of Dunham (1962).

3.2.5. Unit V

Interval: 398-U1592B-25R-1, 35 cm, to 26R-2, 85 cm

Thickness: 11.02 m

Depth: 508.75–519.77 mbsf (bottom of hole)

Age: likely Early Pleistocene (see [Biostratigraphy](#))

Lithology: limestone and marble

Unit V was recovered from Hole U1592B and extends from 508.75 mbsf to the bottom of the hole, where drilling ceased (519.77 mbsf) (Table T2). Because drilling was terminated, only the uppermost part of this unit was recovered. Because Hole U1592B was drilled with the RCB system, cores of this unit are severely disturbed by brittle deformation and biscuiting.

The top of this unit (508.75 mbsf) was observed in Section 25R-1 and defined as basement by the first appearance of limestone and marble cobbles below the light gray bioclastic limestone of Unit IV (Figure F14). In the uppermost part of the unit, near the boundary with Unit IV, the limestones and marbles of Unit V are typically reddish yellow due to oxidation. They transition downward to mainly nonoxidized, massive, white, and partly banded limestone and marble (Figure F14). Unit V

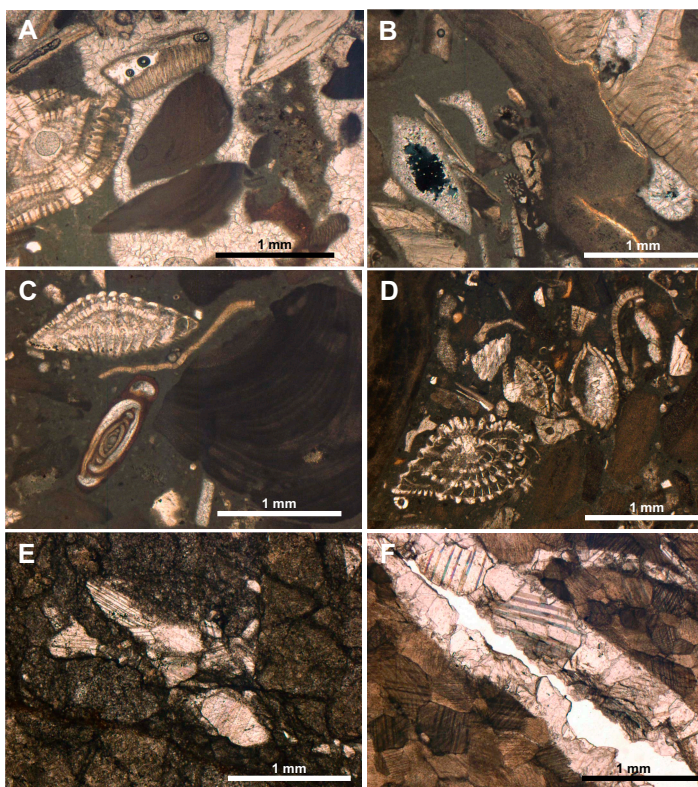


Figure F15. Limestone and marble, Hole U1592B. A–D. Unit IV matrix- to clast-supported bioclastic limestone containing component (allochemical) particles of predominantly bioclasts including benthic and planktonic foraminifera, bivalves, gastropods, corals, and algae. Minor lithic components, including sedimentary and metamorphic rock types, were also observed. Matrices either (A) consist of sparry calcite cement or (B–D) are micritic (A: 24R-1, 16–19 cm; B: 24R-2, 71–74 cm; C, D: 24R-2, 10–14 cm). E, F. Unit V (E) crystalline limestone (26R-2, 11–14 cm) and (F) granular calcite marble (26R-2, 62–65 cm).

is interpreted as the basement to the overlying sedimentary packages in Units I–IV. Compared to Unit IV, this unit is marked by slightly reduced *P*-wave velocities, similar low MS and NGR, and higher thermal conductivity (see **Physical properties**).

Thin sections of two samples from this unit show crystalline limestone (Figure **F15E**) and white, partly banded, granular calcite marble (Figure **F15F**).

3.3. Correlations between holes

Hole U1592B was drilled to overlap with the base of Hole U1592A so that the recovered stratigraphy could be correlated. Hole U1592A extends to 338.35 mbsf and Hole U1592B recovery begins at 293 mbsf, so ~45 m of overlap was recovered. This allows for correlation of several sediment-specific features such as organic-rich sediments and lithic-rich layers between the base of Hole U1592A and the beginning of Hole U1592B.

3.3.1. Notable correlated deposits

- Interval 398-U1592A-50X-2, 25–97 cm (308.88–309.57 mbsf): dark reddish brown tuffaceous ooze transitions downward into a greenish gray ooze and then a black lithic sand (Figure **F16A**). A similar lithology sequence is observed in Hole U1592B intervals 3R-5, 90–101 cm, and 3R-6, 0–48 cm (308.55–309.14 mbsf). Moderate bioturbation is observed in both tuffaceous sediments at the tops of these intervals. The lower 4 cm of the tuffaceous ooze in Hole U1592A is thinly laminated, which is not observed in the same interval in Hole U1592B; however, this small interval may have been lost due to drilling disturbance. Similarly, the lithic-rich interval in Hole U1592A is thicker than that in Hole U1592B. A crack in the core at this point caused by drilling disturbance may have caused some lithics to be lost during recovery.
- Interval 398-U1592A-51X-1, 0–54 cm (316.8–317.52 mbsf): biscuitied, gray, very fine-grained (clay-sized) ooze. A similar lithology is observed in Hole U1592B interval 4R-3, 0–62 cm (314.71–315.33 mbsf), although this section is intact. We tentatively correlate these two intervals (Figure **F16B**).

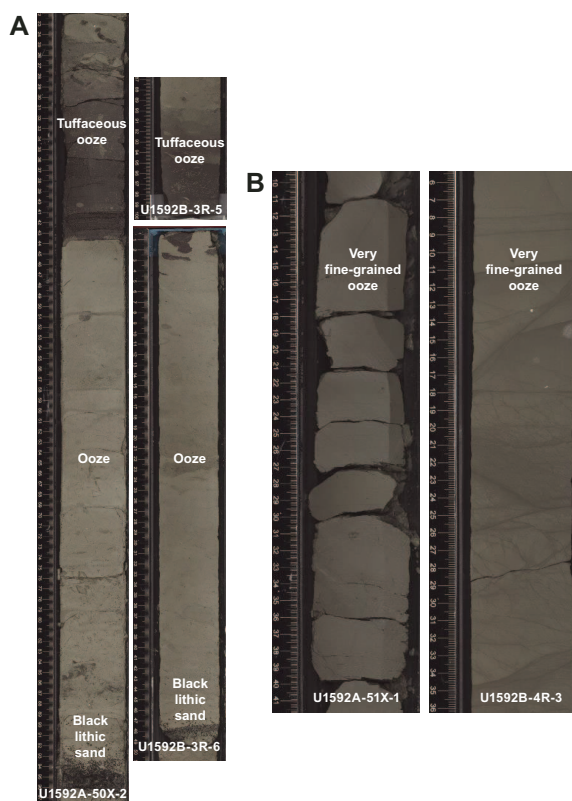


Figure F16. A, B. Unique stratigraphic sections in Hole U1592A that correlate to Hole U1592B.

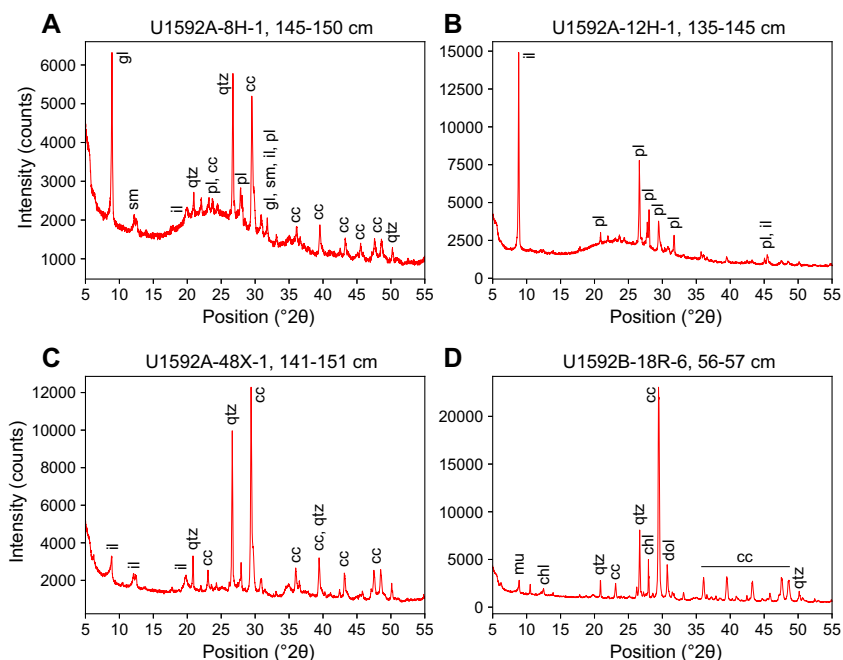


Figure F17. Selected XRD spectra of Unit I–III lithologies, Site U1592. A. Tuffaceous ooze, Unit I. B. Volcanic ash, Unit I. C. Ooze, Unit II. D. Dolomitic sand, Unit III. gl = glauconite, sm = smectite (montmorillonite), il = illite, qtz = quartz, pl = Ca-rich plagioclase, cc = calcium carbonate (calcite, aragonite), mu = muscovite, chl = chlorite, dol = dolomite.

3.4. X-ray diffraction

XRD data were collected from 18 interstitial water (IW) squeeze cake sediment residues from Hole U1592A and 13 from Hole U1592B. The analyzed samples comprise lithologies from Lithostratigraphic Units I–III. Additionally, one more sample was analyzed from Unit III from Hole U1592B. No XRD data were obtained on lithologies from Units IV and V.

Tuffaceous and volcanic lithologies (Figure F17A, F17B) show a characteristic hump at low $^{\circ}2\theta$, indicating the presence of volcanic glass. Mineral phases in tuffaceous lithologies include Ca-rich plagioclase and, depending on the proportion of volcanic to nonvolcanic material, a range of other phases such as quartz, calcium carbonate (calcite and aragonite), clay minerals typical of the illite group and smectite group (montmorillonite), and glauconite. Volcanic ash samples typically have peaks characteristic of Ca-rich plagioclase, occasionally accompanied by clay minerals of the illite group and in some cases rare quartz. XRD spectra of oozes (Figure F17C) are typically dominated by calcium carbonate (calcite and aragonite), quartz, and clay minerals of the illite group. A distinguishing feature of the nonvolcanic sediments (sands and oozes) of Unit III (Figure F17D), compared to Unit I and Unit II lithologies, is the relatively high proportion of dolomite, which was detected in all but one sample from Unit III. Relative proportions of dolomite in Unit III lithologies, as determined using the Rietveld method, range 3.9%–31.9%, although with the exception of a few analyzed samples, calcite and/or aragonite remain the most abundant carbonate phases.

4. Stratigraphic correlation

Two holes were drilled at Site U1592. Hole U1592A was drilled to 338.38 mbsf using the APC (0–137.52 mbsf) and HLAPC systems (137.5–272.62 mbsf) as well as the XCB system (273.8–338.38 mbsf). Hole U1592B was drilled using the RCB system (293–519.78 mbsf). No correlation during coring was required because Hole U1592A already proved to be very challenging for drilling and the priority for Hole U1592B was to advance to the basement without any delay. Therefore, we did not use the Special Task Multisensor Logger (STMSL) for measurements of physical properties to establish fast correlations.

Both holes had only a short overlap, which restricted stratigraphic correlation to the interval between 293 and 338.38 mbsf (Figure F18). Here, we identified several correlations mainly based on the MS and NGR measurements derived with the Whole-Round Multisensor Logger (WRMSL) and the Natural Gamma Radiation Logger (NGRL) as well as half-core images. Correlations were identified between the following cores:

- 398-U1592A-49X and 398-U1592B-2R,
- 398-U1592A-49X and 398-U1592B-3R,
- 398-U1592A-50X and 398-U1592B-3R,
- 398-U1592A-52X and 398-U1592B-5R,
- 398-U1592A-53X and 398-U1592B-5R,
- 398-U1592A-53X and 398-U1592B-6R, and
- 398-U1592A-55X and 398-U1592B-6R.

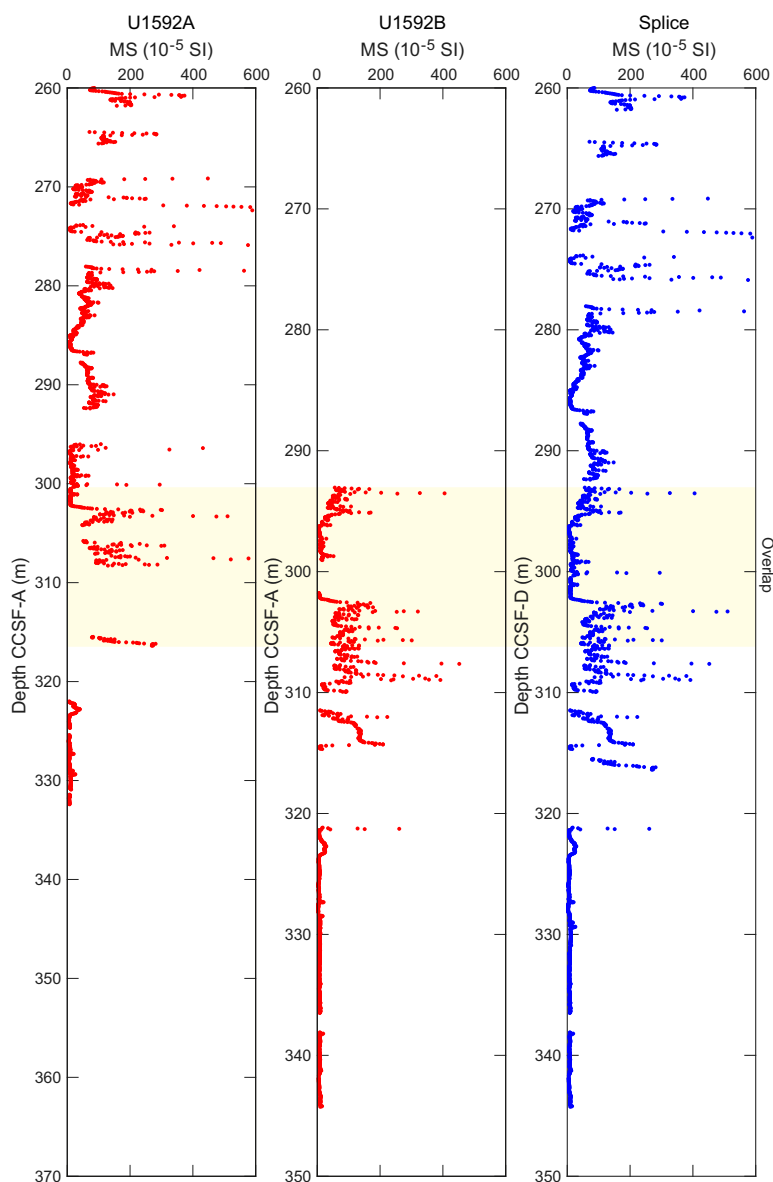


Figure F18. WRMSL-derived MS data, Holes U1592A and U1592B. Note that MS data are on the CCSF-A depth scale and the spliced section (right) is on the CCSF-D depth scale. Yellow shading = overlapping depth sections.

We used these correlations to determine affine ties between the two holes (Table T3) and applied some minor shifts to the cores that did not exceed 6 m. All cores from Hole U1592A above 287 mbsf were not shifted, whereas all cores from Hole U1592B below 339.2 mbsf were shifted by a constant distance of 3.5 m to correlate Holes U1592A and U1592B above 339.2 mbsf. The resulting splice is reported in Table T4. Figure F19 shows the MS, NGR, and gamma ray attenuation (GRA) density measurements on the core composite depth below seafloor, Method D (CCSF-D), scale as well as the coverage of respective core depth intervals with Holes U1592A and U1592B.

Table T3. Affine ties, Site U1592. [Download table in CSV format.](#)

Table T4. Splice ties, Site U1592. [Download table in CSV format.](#)

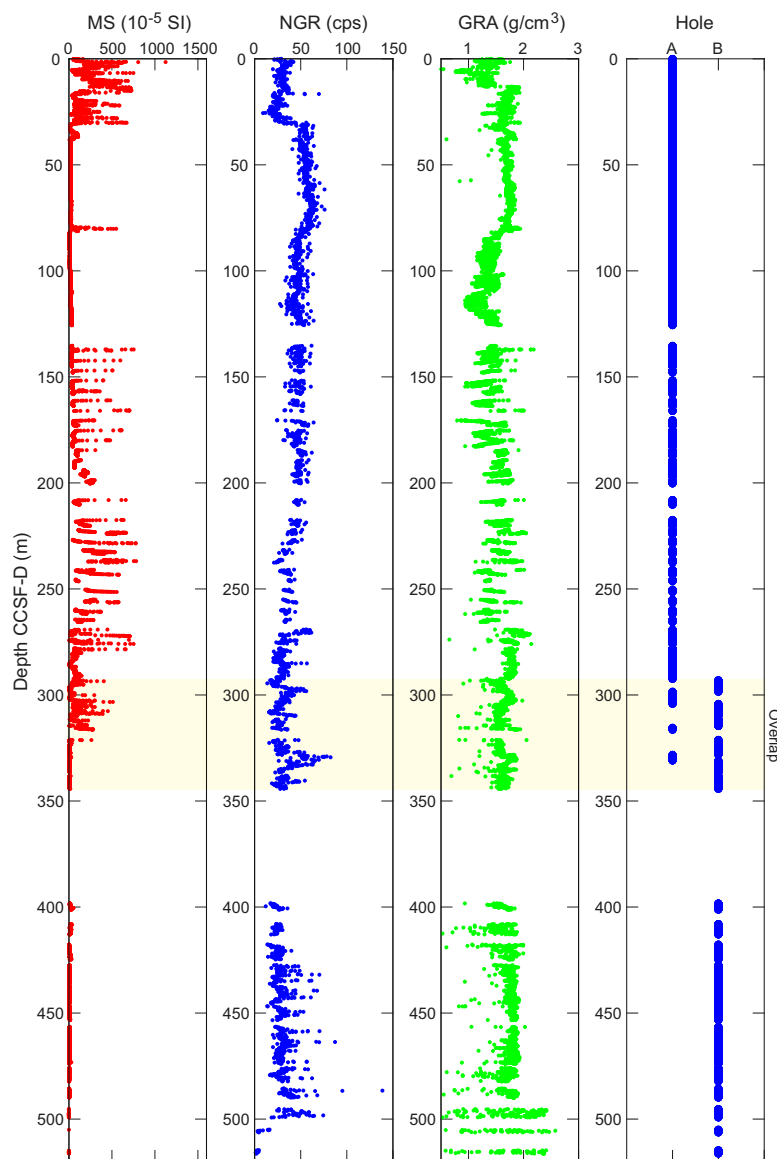


Figure F19. Splice, Site U1592. MS, NGR, and GRA density, as well as the respective spliced core interval from Holes U1592A and U1592B, are shown. cps = counts per second. Yellow shading = overlapping depth sections.

5. Structural geology

Structural geology analyses at Site U1592 included description of cores retrieved from Holes U1592A and U1592B. A total of 323 structures were measured, most derived from relatively consolidated intervals. Observed and measured structures on cores include bedding (20.7%), faults (36.2%), deformation bands (42.7%), and sediment veins (0.3%). The distributions of the dip angles of planar structures are shown in Figure F20, measured with an estimated accuracy of $\pm 2^\circ$. Deformation related to drilling and core recovery was noted but not recorded. Here, we describe and provide examples of each of the features that were recorded.

5.1. Bedding

Bedding planes ($n = 67$) were measured mainly on thin sand beds/laminae, oozes, and micrite boundaries. They mostly exhibit horizontal to subhorizontal dips throughout the core (Figure F20). However, some steeper dips are observed that are associated with slumping or faulting (blue shading in the figure).

Because of large sections of liquefied volcanoclastic deposits (between ~ 50 and 270 mbsf) and poor core recovery (between ~ 350 and 400 mbsf), structure measurements are discontinuous at this site. Thus, the available bedding measurements were divided according to lithostratigraphic units/subunits, as defined by core description (see **Lithostratigraphy**), and box plots were used to indicate the distribution of bedding dips (Figure F21). Measurements were mostly concentrated in Lithostratigraphic Subunits Ib–Ic and Units II and III (Figure F20), dividing the data into three units. In the figure, each box indicates the data distribution range between the twenty-fifth and seventy-fifth percentiles, which is statistically meaningful. Median values (fiftieth percentile of all respective measurements in a unit), which are representative of the data distribution, were used for the evaluation of dip angles.

A decrease in bedding dip was identified between Unit III (median dip = 7.0°) and Unit II (median dip = 4.5°). In contrast, from Unit II to Subunits Ib–Ic, the median dip increased from 4.5° to 7.0° (Figure F21). Unit II features ooze-dominated deposits, whereas Subunits Ib–Ic feature interbed-

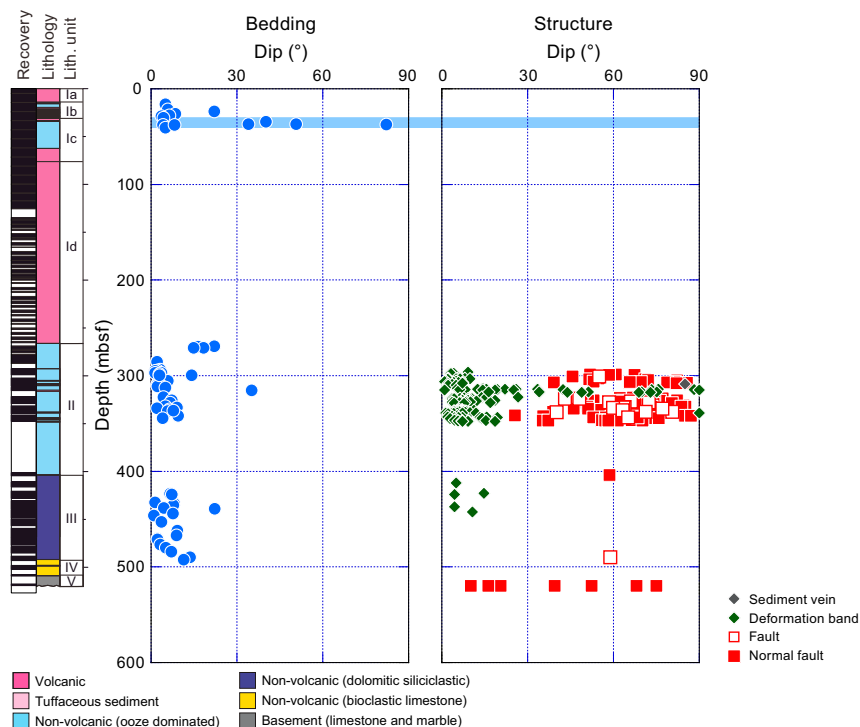


Figure F20. Dip data, Site U1592. Blue shading = development of slumps.

ded volcanic/tuffaceous and ooze deposits (see [Lithostratigraphy](#)). Tectonic shaking and/or the occurrence of volcanism triggered slumps in Subunits Ib–Ic, resulting in increased median dips within the twenty-fifth to seventy-fifth percentile (Figures [F21](#), [F22](#)).

5.2. Slumps

A slump deposit was identified in the upper part (31–38 mbsf) of Hole U1592A (Figure [F22](#)), indicated by scattered distribution of bedding dips in this interval (Figure [F20](#)). The lower part of the slump showed a recumbent fold axis covered by relatively softer, poorly sorted muddy sand. The top of the sand layer overlying the slump was identified at Section 4H-5, 75 cm (31 mbsf), whereas the bottom of the slump was at Section 5H-3, 115 cm (38 mbsf).

5.3. Faults

A large population of normal faults and deformation bands developed in the interval 300–350 mbsf (Figures [F20](#), [F23](#)). The normal faults show displacements of more than a few millimeters. The sense and/or amount of displacement is defined where the normal faults cut bioturbation or sedimentary structures and by the geometry of slickensteps on fault surfaces. Faults at Site U1592 have a normal sense of displacement only and mostly represent cohesive (healed) fault planes with closed fault planes. However, some of the normal faults have open fault planes with slickenlines and slickensteps.

Dark-colored deformation bands, roughly planar and 0.1–2 mm wide, are densely developed in the interval 300–350 mbsf (Figure [F20](#)). These bands were observed in clay-rich intervals without bioturbation. On the split core surface of Section 398-U1592B-4R-2 (Figure [F24](#)), deformation bands form an anastomosing pattern with crosscutting relationships. The sense of slip was always normal when identifiable. Deformation bands are well developed at plate subduction zones and recovered by the Deep Sea Drilling Project and the Ocean Drilling Program in the Nankai accretionary margin (e.g., Maltman et al., 1993; Maltman, 1998; Ujiie et al., 2004), Chile (Rochford et al., 1995), and Costa Rica (Vannucchi and Tobin, 2000). These examples of deformation bands, however,

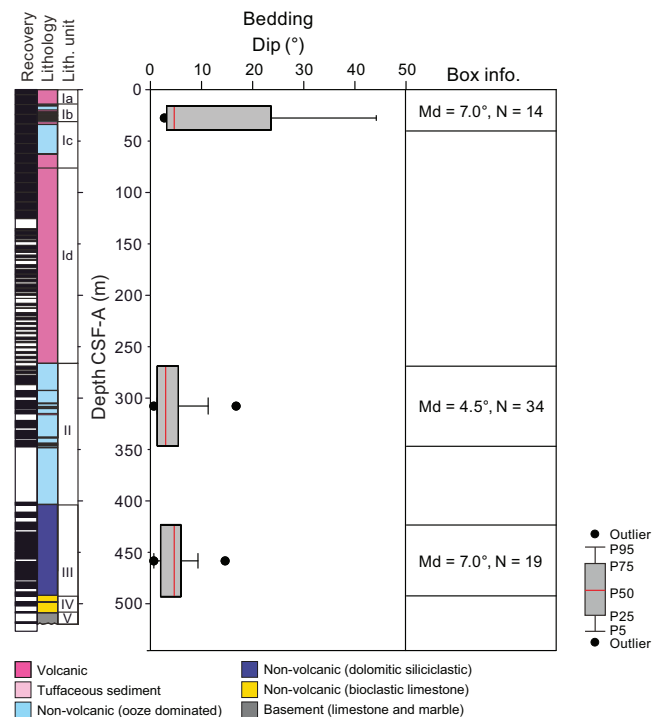


Figure F21. Box plots of bedding dip distribution, Site U1592. The minimum (P5), first quartile (P25), median value (P50), third quartile (P75), and maximum (P95) are shown. Only the first outlier smaller than P5 and larger than P95 is plotted as a dot. Md = median dip, N = number of samples.

show a reverse sense of slip. Normal-fault-induced deformation bands at Site U1592 are therefore a unique example.

Between 300 and 350 mbsf at Site U1592 is a ~50 m interval with no recovery, possibly composed of unstable pumice-rich materials. Below that (400–508 mbsf) in Lithostratigraphic Unit III, the population of faults and deformation bands drastically decreased despite good core recovery

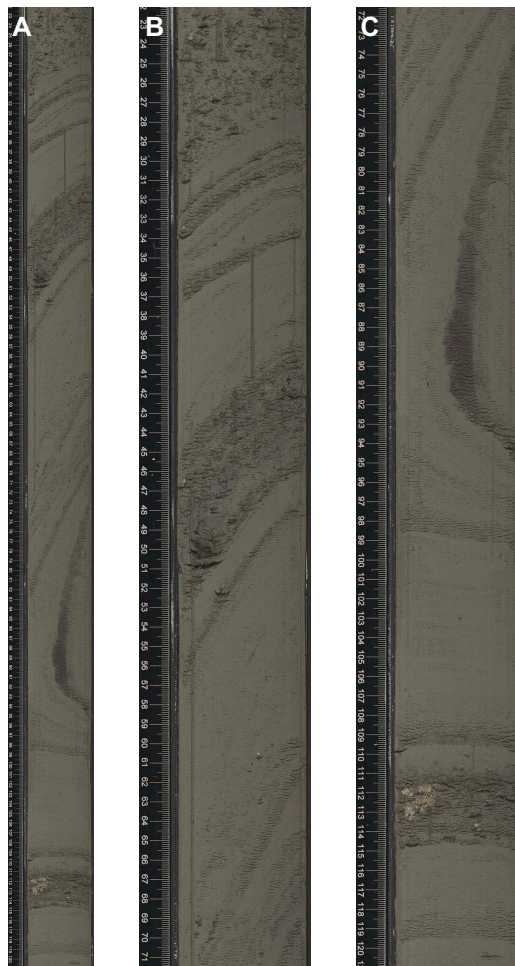


Figure F22. Slump, Hole U1592A. A. Lower part of the slump exhibiting a fold (5H-3, 22–21 cm). B. 5H-3, 22–71 cm. C. 5H-3, 71–121 cm.

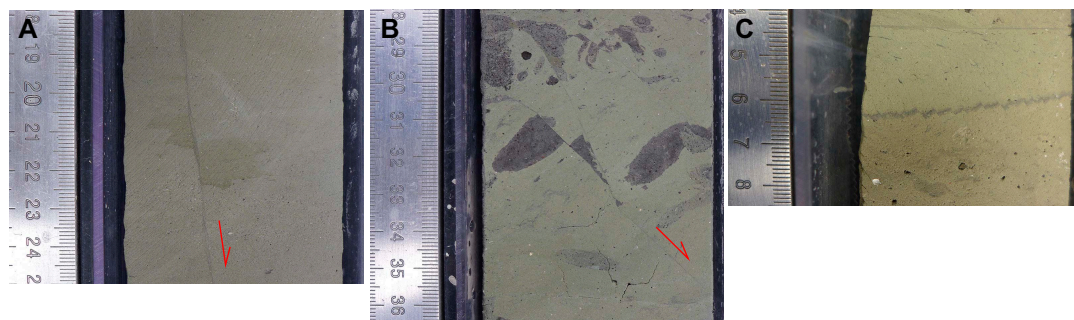


Figure F23. Normal faults, Site U1592. Normal faults and deformation bands occurred in dense population at 300–350 mbsf. Arrows = positions of faults and sense of shear direction. A, B. Normal faults identified just below slump layers (A: 398-U1592B-3R-5, 18–25 cm; B: 398-U1592A-49X-1, 28–36 cm). C. Systematic pattern of normal faulting (398-U1592A-50X-1, 4–8 cm).

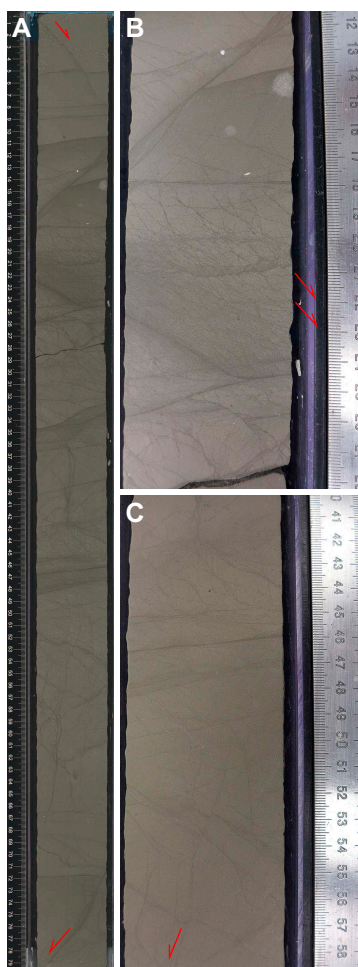


Figure F24. Deformation bands, Section 398-U1592B-4R-2. A. Deformation bands represent offset showing normal sense of shear and were observed in clay-rich intervals that lack bioturbation. Range in thickness was <2 mm. Arrows = positions of faults and sense of shear direction. B. 11.5–28.5 cm. C. 40–59 cm.

(Figure F20). Therefore, the intense deformation, mostly associated with normal faulting, was developed only in this interval (300–350 mbsf). In other words, the normal faulting and deformation bands apparently relate to the gravitational instability closer to the assumed pumice-rich interval, or they were merged into a detachment fault developed in the interval.

Around 519 mbsf at Site U1592, some normal faults developed in marble in Unit V.

6. Biostratigraphy

Calcareous nannofossils and planktonic and benthic foraminifera were examined from core catcher samples and additional split core samples from Holes U1592A and U1592B to develop a shipboard biostratigraphic framework for Site U1592. Additionally, planktonic and benthic foraminifera provided data on paleowater depths, downslope reworking, and possible dissolution.

Site U1592 cored the Anafi Basin sedimentary sequence and upper portion of the limestone and marble basement, recovering a 518.92 m thick Holocene to Early Pleistocene sequence of variable lithology. Calcareous nannofossils and planktonic foraminifera provided good age control in the Holocene through Early Pleistocene sediments. Ages were not provided by benthic foraminifera due to the absence of biostratigraphic markers, likely as a result of unfavorable environmental conditions. Additionally, because of the high sedimentation rates throughout much of the cored section, semiquantitative planktonic foraminiferal assemblage data were used in conjunction with

calcareous nannofossil and planktonic foraminiferal biostratigraphic datums to tentatively assign marine isotope stage boundaries. These are based primarily on fluctuations of the warm-water species *Globigerinoides ruber*, *Globigerinoides elongatus*, and *Globigerinoides pyramidalis* (see Aze et al., 2011; Crundwell et al., 2008; Crundwell and Woodhouse, 2022; Woodhouse et al., 2023). Biostratigraphic datums recognized at Site U1592 are given in Tables T5 and T6, and an age-depth plot is shown in Figure F25.

In Hole U1592A, Holocene to Early Pleistocene sediments (0 to ~0.91 Ma) were recovered from Samples 1H-CC, 16–18 cm, to 55X-CC, 7–10 cm (5.10–338.38 mbsf). Hole U1592B recovered Early Pleistocene sediments (~0.91–1.82 Ma) from Samples 2R-CC, 19–21 cm, to 25R-1, 26–28 cm (299.32–508.67 mbsf). Throughout the entire cored interval, consistent reworking of microfossils sourced from Pleistocene–Early Cretaceous sediments was observed, where reworked Eocene larger benthic foraminifera constituted a substantial bioclastic component of Lithostratigraphic Unit IV (493.5–508.75 mbsf).

6.1. Calcareous nannofossils

The calcareous nannofossil biostratigraphy in Holes U1592A and U1592B was established through analysis of core catcher samples and additional split core samples. Nannofossils are common to abundant in samples from the Middle to Late Pleistocene sequence (Hole U1592A: 5.09–338.365 mbsf; Hole U1592B: 299.31–508.67 mbsf). Preservation is generally good to moderate with sporadically poor intervals throughout the sequence (Figures F25, F26); however, there is significant reworking of older material in most of the Pleistocene samples. The assemblages are characterized

Table T5. Calcareous nannofossil events and absolute ages, Site U1592. [Download table in CSV format.](#)

Calcareous nannofossil event	Age (Ma)	Top core, section, interval (cm)	Bottom core, section, interval (cm)	Top depth CSF-A (m)	Mid-depth CSF-A (m)	Bottom depth CSF-A (m)
		398-U1592A-	398-U1592A-			
Base <i>Emiliana huxleyi</i>	0.265	3H-CC, 23–25	4H-CC, 6–8	24.51	29.015	33.52
Top <i>Gephyrocapsa</i> sp. 3	0.61	52X-CC, 20–22	53X-CC, 17–19	329.51	333.15	336.79
		398-U1592B-	398-U1592B-			
Top <i>Gephyrocapsa</i> sp. 3	0.61	4R-CC, 12–14	5R-CC, 21–23	315.85	322.635	329.42
Base <i>Gephyrocapsa</i> sp. 3	0.97	16R-CC, 23–25	17R-CC, 20–23	428.51	434.20	439.89
Base <i>Reticulofenestra asanoi</i>	1.078	17R-CC, 20–22	18R-CC, 11–13	439.91	444.54	449.17
Top large form (>5.5 µm) <i>Gephyrocapsa</i> spp.	1.245	19R-CC, 25–27	20R-CC, 11–13	457.11	463.365	469.62
Base large form (>5.5 µm) <i>Gephyrocapsa</i> spp.	1.617	21R-CC, 7–9	23R-CC, 10–12	477.51	485.495	493.48
Top <i>Calcidiscus macintyre</i>	1.664	21R-CC, 7–9	23R-CC, 10–12	477.51	485.495	493.48

Table T6. Foraminiferal events and absolute ages, Site U1592. [Download table in CSV format.](#)

Foraminifer event	Age (Ma)	Top core, section, interval (cm)	Bottom core, section, interval (cm)	Top depth CSF-A (m)	Mid-depth CSF-A (m)	Bottom depth CSF-A (m)
		398-U1592A-	398-U1592A-			
Planktonic foraminifera						
Base <i>Globigerinoides ruber</i> pink	0.33	4H-CC, 6–8	5H-CC, 19–21	33.52	38.525	43.53
Paracme top <i>Neogloboquadrina</i> spp. (sin)	0.51	47X-CC, 42–47	48X-CC, 20–25	287.48	290.085	292.69
		398-U1592B-	398-U1592B-			
Paracme base <i>Neogloboquadrina</i> spp. (sin)	0.91	3R-CC, 19–21	4R-CC, 12–14	311.21	313.53	315.85
Top influx <i>Truncorotalia crassaformis</i>	1.12	17R-CC, 20–22	18R-CC, 11–13	439.91	444.54	449.17
Base influx <i>Truncorotalia crassaformis</i>	1.15	18R-CC, 11–13	19R-CC, 25–27	449.17	453.14	457.11
Paracme top <i>Neogloboquadrina</i> spp. (sin)	1.21	18R-CC, 11–13	19R-CC, 25–27	449.17	453.14	457.11
Top <i>Globigerinoides obliquus</i>	1.28	19R-CC, 25–27	20R-CC, 11–13	457.11	463.365	469.62
Paracme base <i>Neogloboquadrina</i> spp. (sin)	1.37	19R-CC, 25–27	20R-CC, 11–13	457.11	463.365	469.62
Base common <i>Neogloboquadrina</i> spp. (sin)	1.79	20R-CC, 11–13	21R-CC, 7–9	469.62	473.565	477.51
Top rare <i>Globigerinoides obliquus</i>	1.82	21R-CC, 7–9	23R-CC, 10–12	477.51	485.495	493.48
		398-U1592A-	398-U1592A-			
Marine isotope stage boundaries						
Base MIS10	0.374	28F-CC, 14–16	29F-CC, 10–12	193.09	195.115	197.14
Base MIS11	0.424	37F-CC, 19–21	38F-CC, 15–17	233.77	235.785	237.80

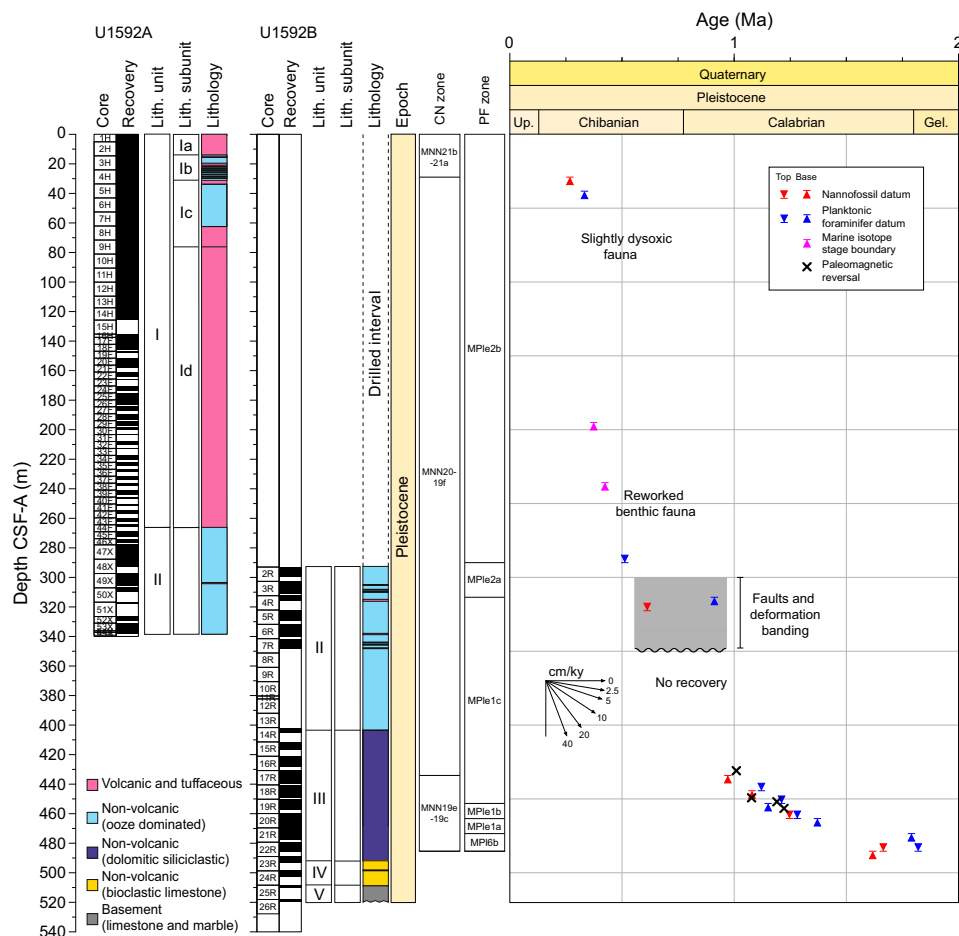


Figure F25. Age-depth plot, Holes U1592A and U1592B. Integrated biochronology, magnetostratigraphy, and marine isotope stage boundaries are shown. CN = calcareous nannofossil, MNN = Mediterranean Neogene Nannoplankton, PF = planktonic foraminifer. Biohorizons correspond to those in Tables T5 and T6.

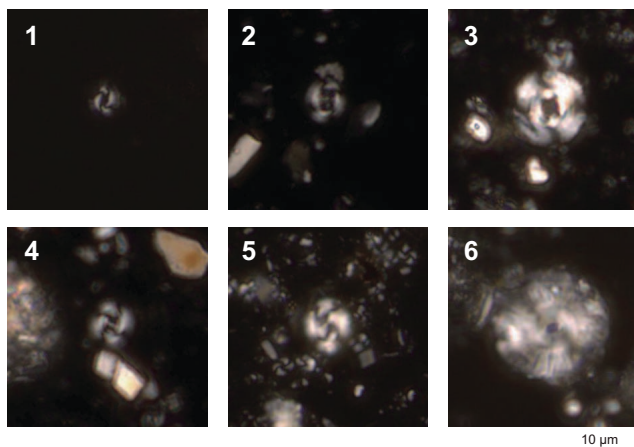


Figure F26. Calcareous nannofossils, Site U1592. 1. *Emilia huxleyi* (Lohmann) Hay and Mohler (398-U1592A-1H-CC, 16–18 cm). 2. *Gephyrocapsa* sp. 3 (53X-CC, 17–19 cm). 3. *Reticulofenestra asanoi* Sato and Takayama (398-U1592B-16R-CC, 10–12 cm). 4. *Gephyrocapsa oceanica* Kamptner (398-U1592A-54X-CC, 34–37 cm). 5. *Gephyrocapsa* spp. large form (>5.5 µm) (398-U1592B-20R-CC, 11–13 cm). 6. *Calcidiscus macintyreii* (Bukry and Bramlette) Loeblich and Tappan (23R-CC, 20–23 cm).

by the occurrence of warm-water species such as *Rhabdosphaera clavigera* and *Umbilicosphaera sibogae* throughout the sequences in Holes U1592A and U1592B.

Seven nannofossil biostratigraphic datums are recognized at Site U1592, representing a continuous Middle to Late Pleistocene sedimentary sequence. The distribution of calcareous nannofossil taxa is shown in Tables **T5** and **T6**, and biostratigraphic datums are given in Table **T7**.

The presence of *Emiliania huxleyi* in Samples 398-U1592A-1H-CC, 16–18 cm, to 3H-CC, 23–25 cm (5.09–24.51 mbsf), indicates a Holocene to Middle Pleistocene age (≤ 0.265 Ma) in Zones MNN21a and 21b (CNPL11, Backman et al., 2012; NN21, Martini, 1971; CN15, Okada and Bukry, 1980) of Rio et al. (1990) and Di Stefano and Sturiale (2010). The top occurrence of *Gephyrocapsa* sp. 3 (0.61 Ma), situated between the lower part of the Brunhes Chron in Zone MNN19f, is found between Samples 52X-CC, 20–22 cm, and 53X-CC, 17–19 cm (329.51–336.79 mbsf), and between Samples 398-U1592B-4R-CC, 12–14 cm, and 5R-CC, 21–23 cm (315.85–329.42 mbsf). The basal occurrence of *Gephyrocapsa* sp. 3 (0.97 Ma), situated between the top of the Jaramillo Subchron of the Matuyama Chron in Zone MNN19e, is found between Samples 16R-CC, 23–25 cm, and 17F-CC, 20–23 cm (428.51–439.89 mbsf). The basal occurrence of *Reticulofenestra asanoi* (1.078 Ma), which lies just below the Jaramillo Subchron of the Matuyama Chron in Zone MNN19e, is found between Samples 17R-CC, 20–22 cm, and 18R-CC, 11–13 cm (439.91–449.17 mbsf). The large form of *Gephyrocapsa* spp. (>5.5 μm) that appears between 1.245 and 1.617 Ma (Zones MNN19d, CNPL8, NN19, and CN13b) occurs in Samples 20R-CC, 11–13 cm, and 21R-CC, 7–9 cm (469.63–477.5 mbsf). The top of *Calcidiscus macintyreii* (1.664 Ma), which is correlated to the Zone MNN19b/19c boundary, is recognized between Samples 21R-CC, 7–9 cm, and 23R-CC, 10–12 cm (477.51–493.48 mbsf). The assemblage in Sample 25R-1, 27 cm (508.67 mbsf), is characterized by the occurrence of *Gephyrocapsa* spp. (small form), *Pseudoemiliania lacunosa*, and *Reticulofenestra* spp. and lack of Discoasteraceae. Thus, Sample 25R-1, 27 cm, is tentatively placed in Zone MM19a (1.73–1.95 Ma).

6.2. Foraminifera

Planktonic and benthic foraminifera were examined from core catcher samples and split core samples from Holes U1592A and U1592B. Absolute ages assigned to biostratigraphic datums follow those listed in Table **T5** in the Expedition 398 methods chapter (Kutterolf et al., 2024). Planktonic foraminifer datums are given in Table **T5**, and the distributions of planktonic and benthic foraminifer taxa are given in Tables **T8** and **T9**. Planktonic foraminifer abundances and indications of oceanicity (e.g., Hayward et al., 1999) and benthic foraminifer paleowater depth estimations are shown in Figures **F27** and **F28**.

Because of the volcanogenic nature of the cored sedimentary sequence, residues (>125 μm) from washed samples were often significantly composed of volcanoclastic particles such as pumice, scoria, and ash that often diluted the microfossil component of residues. Foraminifera dominated the biogenic component of residues, however, and age markers were present in sufficient numbers to date most samples reliably. As well as volcanic material, clastic grains, minor pyrite, carbonaceous plant-derived matter, and other fossil material including shells and fragments (Bivalvia and Gastropoda), Pteropoda, Scaphopoda, Bryozoa, Arthropoda (*Balanus*), echinoid spines and plate fragments, and ostracods, as well as fish vertebrae, were also present in variable amounts in most samples. In addition, reworked Pliocene foraminifera were often present.

In the Holocene to Early Pleistocene section, foraminifera with very good to very poor preservation are present in siliciclastic and volcanoclastic sediments. Preservation was generally very good except for the lower part of Hole U1592B, where preservation was notably poorer in Samples 14R-

Table T7. Distribution of calcareous nannofossils, Site U1592. [Download table in CSV format.](#)

Table T8. Distribution of planktonic foraminifera, Site U1592. [Download table in CSV format.](#)

Table T9. Distribution of benthic foraminifera, Site U1592. [Download table in CSV format.](#)

Core, section, interval (cm)	Bottom depth CSF-A (m)	AW Planktonic (%)	OK Planktonic (%)	Planktonic mean (%)	Oceanicity	Paleowater depth (m)	
398-U1592A-							
1H-CC	5.10	100	50	75	Sub-oceanic	NA	NA
2H-CC	14.54	44	50	47	Extra-neritic	Upper to mid bathyal	400-800
3H-CC	24.51	91	80	85.5	Sub-oceanic		
4H-CC	33.54	93	86	89.5			
5H-CC	43.53	79		79		NA	NA
6H-CC	52.93	100	83	91.5	Oceanic	Slightly dysoxic conditions	
7H-CC	62.64	42	70	56	Extra-neritic		
8H-CC	72.11	74	80	77	Sub-oceanic		
9H-CC	81.52	85	90	87.5			
10H-CC	90.68	96	80	88			
11H-CC	99.94	95	80	87.5	Oceanic	NA	NA
12H-CC	109.18	97	95	96			
13H-CC	117.55	98	90	94	Sub-oceanic	Upper to mid bathyal	400-800
14H-CC	125.81	94	90	92			
16H-CC	137.52	93	82	87.5			
17F-CC	141.77	92	95	93.5			
18F-CC	145.71	87	69	78			
19F-CC	148.15	80	73	76.5			
20F-CC	155.86	82	78	80			
21F-CC	158.25	76	82	79			
22F-CC	163.90	79	62	70.5			
23F-CC	166.21	88	66	77			
24F-CC	173.50	84	85	84.5	Extra-neritic	NA	NA
25F-CC	179.76	89	69	79			
26F-CC	183.16	77	62	69.5	Sub-oceanic	Upper to mid bathyal	400-800
27F-CC	187.37	80	67	73.5			
28F-CC	193.09	79	71	75			
29F-CC	197.14	53	60	56.5			
30F-CC	200.49	56	63	59.5			
31F-CC	203.40	50	63	56.5			
32F-CC	210.49	81	56	68.5			
33F-CC	212.83	61	66	63.5			
34F-CC	220.55	52	57	54.5			
35F-CC	224.38	36	36	36			
36F-CC	228.83	31	32	31.5	Extra-neritic	Reworked benthic	
37F-CC	233.77	38	36	37			
38F-CC	237.80	31	57	44	Sub-oceanic		
39F-CC	243.72	80	61	70.5			
40F-CC	246.48	92	98	95	Oceanic		
41F-CC	251.63	63	92	77.5	Sub-oceanic		
42F-CC	257.10	64	76	70			
43F-CC	262.10	100	75	87.5			
44F-CC	265.87	100	100	100	Oceanic		
45F-CC	272.43	24	22	23	Outer neritic		
46X-CC	276.32	93	89	91	Oceanic	Mid to lower bathyal	700->1000
47X-CC	287.48	81	80	80.5	Sub-oceanic		
48X-CC	292.69	94	88	91	Oceanic		
49X-CC	299.32	93	90	91.5	Sub-oceanic		
50X-CC	305.98	87	85	86			
51X-CC	309.83	51	57	54	Extra-neritic		
52X-CC	311.21	85	90	87.5	Sub-oceanic		
53X-CC	315.85	90	90	90	Oceanic		
54X-CC	318.14	63	57	60	Sub-oceanic		
55X-CC	329.44	85	85	85			
398-U1592B-							
2R-CC	329.51	69	61	65	Sub-oceanic	Slightly dysoxic conditions	
3R-CC	336.57	100	98	99	Oceanic		
4R-CC	336.81	96	85	90.5	Sub-oceanic		
5R-CC	338.38	85	88	86.5			
6R-CC	340.03	82	80	81		NA	NA
7R-CC	348.04				NA	NA	NA
14R-CC	404.96	18	21	19.5	Outer neritic	Mid to lower bathyal	700->1000
15R-CC	416.66	16	15	15.5	Extra-neritic		
16R-3, 102-104	425.12	37	32	34.5			
16R-CC	428.51	91	90	90.5	Oceanic	Upper bathyal to inner shelf	<50 -700
17R-CC	439.91	23	5	14	Inner neritic		
18R-CC	449.19	14	26	20	Outer neritic		
19R-CC	457.11	44	28	36	Extra-neritic		
20R-CC	469.64	34		34			
21R-CC	477.51	27	13	20	Outer neritic		
22R-CC	485.76	6	5	5.5	Inner neritic		
23R-CC	493.50	32	8	20	Outer neritic		

Figure F27. Foraminiferal oceanicity and paleowater depth estimates, Site U1592. Blue colors show relationship between oceanicity index and paleowater depth. Observers: AW = Adam Woodhouse, OK = Olga Koukousioura. NA = not applicable.

CC, 17–22 cm, to 23R-CC, 10–12 cm (404.96–493.5 mbsf). Foraminifer abundances are also highly variable, commonly making up the primary sedimentary component in nannofossil oozes, and are notably rare in more tuffaceous sediments, potentially due to sedimentary dilution, whereas coarser volcanoclastic intervals were sometimes barren.

6.2.1. Holocene to Early Pleistocene biostratigraphy

Because of explosive volcanic events and rapid deposition of the upper sedimentary section, the base of the Holocene is not possible to assign accurately. Planktonic foraminifer assemblages from the Holocene to Early Pleistocene section of Site U1592 are mostly very well preserved, with specimens rarely broken or exhibiting partially dissolved shell walls.

Holocene to Pleistocene foraminifer faunas suggest large fluctuations in relative paleowater depth and oceanicity with highly variable planktonic abundances that range 5.5%–100% when foraminifera were present (Figure F28). The faunas are typical of Pleistocene Mediterranean biostratigraphic zones, primarily composed of *Neogloboquadrina incompta*, *Globigerina bulloides*, *Globigerina falconensis*, *Globigerina umbilicata*, *Globigerinella siphonifera*, *Globigerinita gluti-*

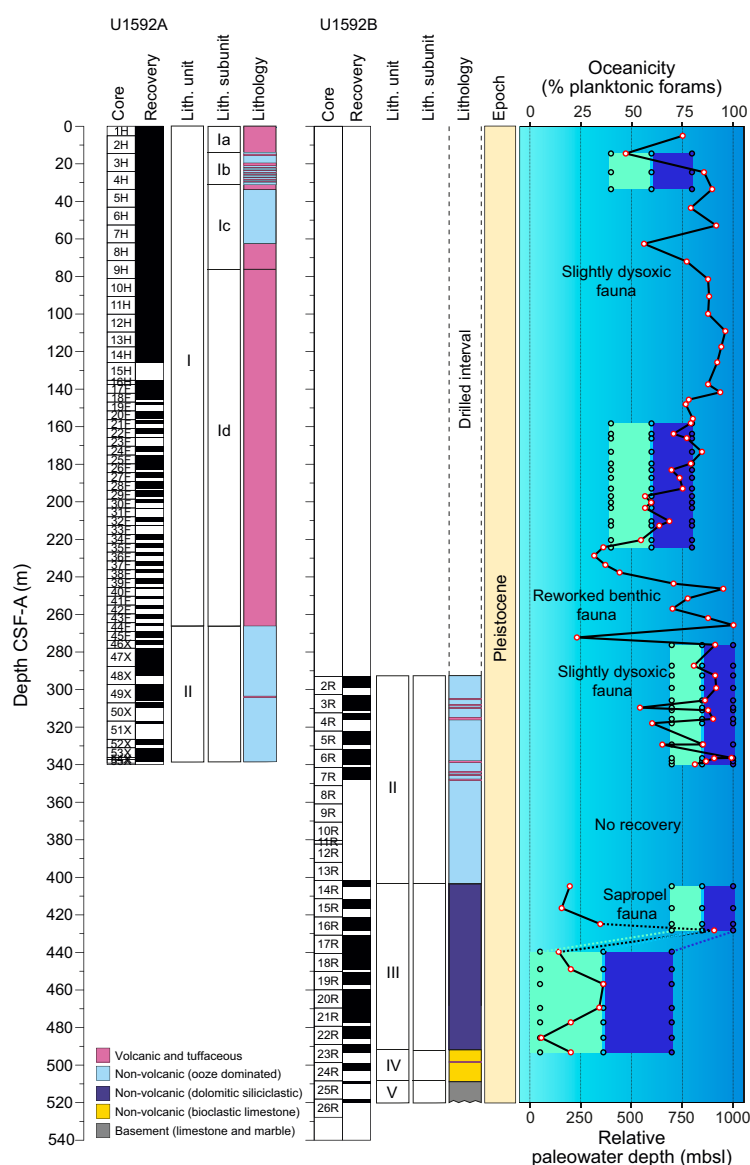


Figure F28. Biostratigraphic summary, Site U1592. Interpreted oceanicity: solid line/red points = interpreted oceanicity, dashed line = extrapolation through barren/unreliable sample data. Interpreted paleowater depths: light blue points/shading = shallower paleowater depths, dark blue points/shading = deeper paleowater depths.

nata, *G. elongatus*, *G. pyramidalis*, *Trilobatus trilobus* group, *G. ruber* var. white, *G.* var. pink, *Globoconella inflata*, *Hirsutella scitula*, *Neogloboquadrina pachyderma*, *Orbulina universa*, *Turborotalita quinqueloba*, and *Globigerinella calida* (Figure F29). Rare reworked specimens of *Globoturborotalita woodi* and *Globoturborotalita decoraperta* are also present throughout section samples.

Foraminiferal faunas are sufficiently common to biostratigraphically divide the Pleistocene into six Mediterranean planktonic foraminiferal biostratigraphic zones (Lirer et al., 2019) bounded by several sedimentary hiatuses:

- Zone MPle2b (0.00–0.53 Ma), Hole U1592A: 5.10–287.48 mbsf.
- Zone MPle2a (0.53–0.94 Ma), Holes U1592A and U1592B: 292.69–311.21 mbsf.
- Zone MPle1c (0.94–1.21 Ma), Hole U1592B: 315.85–449.19 mbsf.
- Zone MPle1b (1.21–1.37 Ma), Hole U1592B: 457.11 mbsf.
- Zone MPle1a (1.37–1.79 Ma), Hole U1592B: 469.64 mbsf.
- Zone MPl6b (1.79–2.00 Ma), Hole U1592B: 477.51–493.50 mbsf.

The faunal criteria on which these age assignments are based are given below.

6.2.1.1. Zone MPle2b (0.00–0.53 Ma)

Samples 398-U1592A-1H-CC, 16–18 cm, to 47X-CC, 42–47 cm (5.10–287.48 mbsf), are assigned to Zone MPle2b based on the paracme top of sinistrally coiled *Neogloboquadrina* spp. (<0.51 Ma) in Sample 47X-CC, 0–5 cm (287.48 mbsf), above which this species is almost continuously present. Furthermore, there are variable occurrences of *Truncorotalia truncatulinoides* (first common occurrence = 0.53 Ma) within this interval, more so than at other sites, likely due to the deeper water (see Schiebel and Hemleben, 2017). Additionally, the first occurrence of *G. ruber* var. pink (<0.33 Ma) occurs in Sample 4H-CC, 6–8 cm.

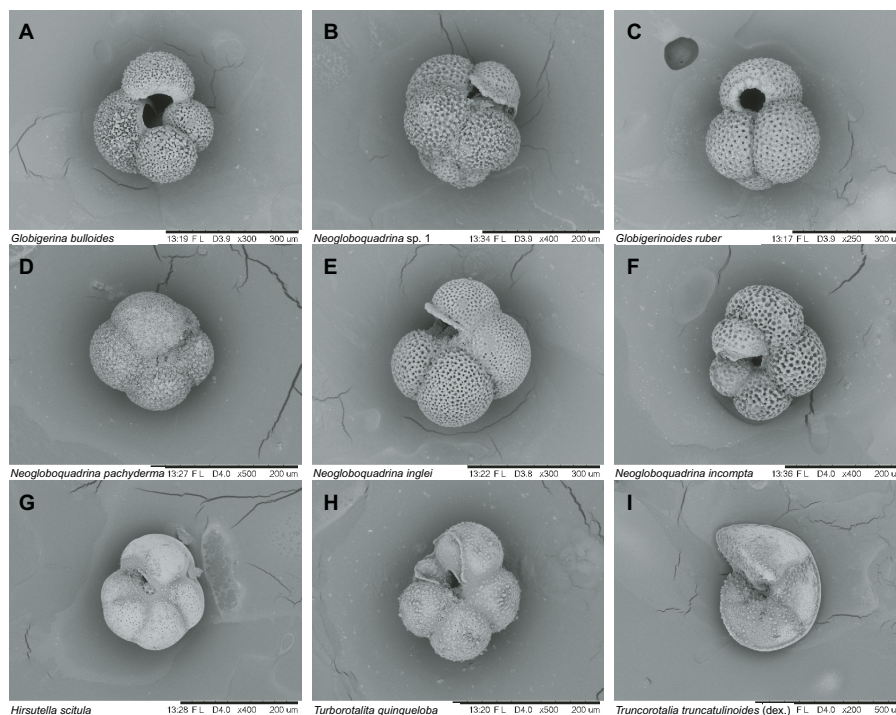


Figure F29. Planktonic foraminifera, Hole U1592A. A. *Globigerina bulloides*. B. *Neogloboquadrina* sp. 1. C. *Globigerinoides ruber*. D. *Neogloboquadrina pachyderma*. E. *Neogloboquadrina inglei*. F. *Neogloboquadrina incompta*. G. *Hirsutella scitula*. H. *Turborotalita quinqueloba*. I. *Truncorotalia truncatulinoides* (dextral). (A, C, E, F, H: 4H-CC, 6–8 cm; B: 11H-CC, 11–15 cm; D, G, I: 13H-CC, 10–15 cm.)

6.2.1.2. Zone MPlE2a (0.53–0.94 Ma)

Samples 398-U1592A-48X-CC, 20–25 cm, to 398-U1592B-3R-CC, 19–21 cm (292.69–311.21 mbsf), are assigned to Zone MPlE2a based on the absence of *T. truncatulinoides* s.l. (0.53–0.934 Ma) and the absence of sinistrally coiled *Neogloboquadrina* spp. (0.51–0.91 Ma) throughout this interval. A very high frequency of deformation banding and normal faulting was identified from ~300 to 350 mbsf (see **Structural geology**) that may represent a hiatus, causing discrepancies within biostratigraphic datums in this interval (Figure F25).

6.2.1.3. Zone MPlE1c (0.94–1.21 Ma)

Samples 398-U1592B-4R-CC, 12–14 cm, to 18R-CC, 11–13 cm (315.85–449.19 mbsf), are assigned to Zone MPlE1c based on the consistently high abundances of sinistrally coiled *Neogloboquadrina* spp. (0.91–1.21 Ma) throughout this interval. Additionally, the influx of *Truncorotalia crassaformis* (1.12–1.15 Ma) was observed in Sample 18R-CC, 11–13 cm (449.19 mbsf).

6.2.1.4. Zone MPlE1b (1.21–1.37 Ma)

Sample 398-U1592B-19R-CC, 25–27 cm (457.11 mbsf), is assigned to Zone MPlE1b based on the low abundance of sinistrally coiled *Neogloboquadrina* spp. (1.21–1.37 Ma) in the sample. Moreover, the sample can potentially be constrained to 1.21–1.28 Ma due to the lack of *Globigerinoides obliquus* s.s. (last occurrence = 1.28 Ma).

6.2.1.5. Zone MPlE1a (1.37–1.79 Ma)

Sample 398-U1592B-20R-CC, 11–13 cm (469.64 mbsf), is assigned to Zone MPlE1a based on the first common occurrence of sinistrally coiled *Neogloboquadrina* spp. (1.37–1.79 Ma) in the sample.

6.2.1.6. Zone MPl6b (1.79–2.00 Ma)

Samples 398-U1592B-21R-CC, 7–9 cm, to 23R-CC, 0–5 cm (477.51–493.50 mbsf), are assigned to Zone MPl6b or older based on the rare occurrences of sinistrally coiled *Neogloboquadrina* spp (>1.79 Ma) and the occurrence of rare *G. obliquus* (>1.82 Ma) and *G. decoraperta* (~1.8 Ma) within this interval. Several carbonate clasts containing biogenic material recovered during coring operations in Lithostratigraphic Unit IV were investigated in thin sections. The clasts (Samples 24R-1, 16–19 cm; 24R-2, 10–14 cm; and 24R-2, 71–74 cm [498.89–500.94 mbsf]) can be assigned to the middle Eocene based on the possible presence of *Nummulites millecaput-maximus* group, *Assilina* sp., *Discocyclus* sp., miliolids, and various undetermined rotaloid forms (Figure F30). However, the occurrence of *G. ruber* (Figure F31) with Early Pleistocene calcareous nannofossils within the matrixes of these deposits suggests reworking of Eocene-aged bioclasts into Lower Pleistocene carbonate sediments.

6.2.2. Planktonic foraminiferal oceanicity

Planktonic foraminifer abundances are highly variable, ranging 5.5%–100% when foraminifera are present (Figures F27, F28). Oceanicity values are generally in good agreement with benthic foraminiferal paleowater depth indicators, indicating suboceanic (200–1000 mbsl) conditions at Site U1592 throughout the majority of the upper cored interval (5.10–340.03 mbsf), and <50–700 mbsf in the lower part (404.96–493.50 mbsf). Notably, the intervals between Samples 398-U1592A-12H-CC, 12–17 cm, and 17F-CC (109.18–141.77 mbsf) and Samples 46X-CC, 29–32 cm, and 398-

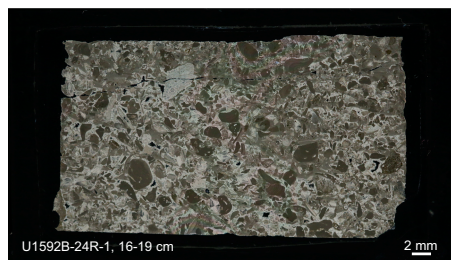


Figure F30. Bioclastic limestone showing possible *Nummulites millecaput-maximus* group, *Assilina* sp., *Discocyclus* spp., miliolids, and various undetermined rotaloid forms, planktonic foraminifera, and mollusks, Hole U1592B.

U1592B-4R-CC, 12–14 cm (276.32–315.85 mbsf), exhibit oceanicity values indicative of potentially deeper waters (open oceanic; deeper than 1000 mbsl) (Figure F28).

6.2.3. Benthic foraminifera paleowater depths

Benthic foraminiferal distributions are highly variable, indicating paleowater depths from inner shelf (<50 m) to lower bathyal (>1000 m) (Figure F28). The low abundances or complete absence of benthic foraminiferal faunas in some samples (e.g., 398-U1592A-36F-CC, 14–16 cm, to 45F-CC, 0–2 cm [228.83–272.43 mbsf]) is possibly correlated with rapid emplacement of volcanoclastic sediments and/or inhospitable environmental conditions. Samples 2H-CC, 24–26 cm, to 4F-CC, 6–8 cm (14.54–33.54 mbsf), and 21F-CC, 8–9 cm, to 35F-CC, 13–14 cm (158.25–224.38 mbsf), record an upper to mid-bathyal (400–800 m) paleowater depth, as indicated by the presence of species such as *Uvigerina peregrina*, *Cassidulina* spp., *Trifarina angulosa*, *Ioanella tumidula*, and *Hyalinea balthica*. Samples 46X-CC, 29–32 cm, to 55X-CC, 7–10 cm (276.32–338.38 mbsf), and 398-U1592B-4R-CC, 12–14 cm, to 16R-CC, 23–25 cm (315.85–428.51 mbsf), exhibit mid- to lower bathyal (700 to >1000 m) paleowater depths, as indicated by the presence of *Oridorsalis umbonatus*, whereas lower bathyal markers including *Cibicidoides wuellerstorfi*, *Cibicidoides mundulus*, and rare occurrences of *Articulina tubulosa* indicate deposition in paleowater depths >1000 mbsl (Figures F28, F32). Common reworked benthic foraminifera in Samples 398-U1592A-36F-CC, 14–16 cm, to 45F-CC, 0–2 cm (228.83–272.43 mbsf), likely represent downslope reworking, whereas in Samples 398-U1592B-17R-CC, 20–22 cm, to 23R-CC, 10–12 cm (439.91–493.5 mbsf), a gradual shallowing of the paleowater depth is recorded from uppermost to upper bathyal (200–700 mbsl) to outer shelf (100–200 m) and finally inner shelf (<50 m). This is indicated by a

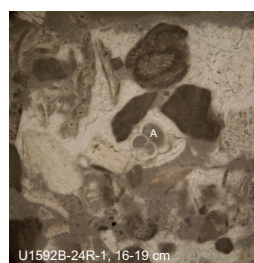


Figure F31. Bioclastic limestone showing possible *Globigerinoides ruber* (A) (plane-polarized light [PPL]).

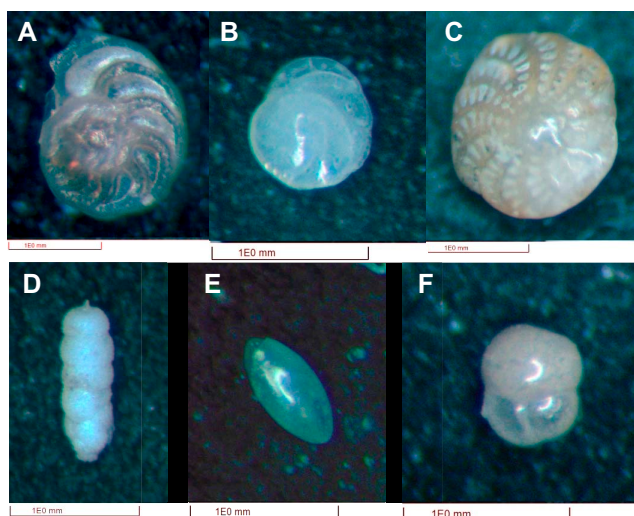


Figure F32. Benthic foraminifera, Site U1592. A. *Cibicidoides wuellerstorfi*, spiral view (398-U1592A-52X-CC, 20–22 cm). B. *Cassidulina carinata*, apertural view (398-U1592B-6R-CC, 0–2 cm). C. *Elphidium crispum*, reworked specimen (398-U1592A-45F-CC, 0–2 cm). D. *Rectuvigerina phlegeri* (11H-CC, 11–15 cm). E. *Chilostomella mediterraneensis* (7H-CC, 16–21 cm). F. *Sphaeroidina bulloides* (398-U1592B-6R-CC, 0–2 cm).

change in fauna from species such as *O. umbonatus* and *Cibicides pachyderma* to typical shelf species and mainly reworked shelf benthic foraminifer fauna.

7. Paleomagnetism

Paleomagnetic analysis at Site U1592 focused on measurement and demagnetization of archive-half sections to determine magnetostratigraphic age controls. The uppermost 82 m of the sequence sampled in Hole U1592A carries normal polarity remanences acquired during the Brunhes Chron (see [Biostratigraphy](#)). Deeper cores recovered from Hole U1592A were unsuitable for paleomagnetic measurement. Interval ~270–348 mbsf in Hole U1592B is also normally magnetized and assigned to the Brunhes Chron. The Brunhes–Matuyama transition (0.773 Ma) was not recovered, but the sequence from 400 to 457 mbsf exhibits changes in magnetic polarity, allowing three reversal boundaries to be tied precisely to the geomagnetic polarity timescale (corresponding to the start/end of the Jaramillo Subchron at 1.008/1.076 Ma and the start of the normal polarity Cobb Mountain Subchron at 1.189 Ma within the Matuyama Chron). An additional tentative correlation to the base of the Cobb Mountain Subchron is also made by reference to a biostratigraphic marker. Samples below 460 mbsf exhibit mainly positive inclinations. However, this unit is dated biostratigraphically to the reversed polarity Matuyama Chron, suggesting that this interval was remagnetized during either the Jaramillo/Cobb Mountain Subchrons or Brunhes Chron.

7.1. Bulk magnetic properties

The bulk magnetic parameters of intensities of magnetization and low-field MS typically have log-normal (geometric) distributions in natural samples (Tarling, 1983). Table [T10](#) provides the geometric means and ranges of these parameters observed at the same measurement points in archive-half sections for both holes cored at Site U1592, whereas the histograms of [Figure F33](#) show their overall distributions for the whole site (plotted as \log_{10} values). Both parameters show several peaks in their distributions, reflecting contributions from variably magnetically susceptible nature of dolomitic siliciclastic sediments, nonvolcanic oozes, and volcanic/tuffaceous sediments.

7.2. Downhole variations in magnetic characteristics

Remanence measurements were made on archive-half section pieces recovered during Expedition 398 by APC and XCB coring in Hole U1592A and RCB coring in Hole U1592B using the 2G Enterprises Model 760R-4K superconducting rock magnetometer (SRM) system. Remanences were measured every 2 cm and were filtered to reject data from points within 8 cm of section ends. This produced a combined site-level data set consisting of natural remanent magnetization (NRM) and

Table T10. NRM intensity and MS, Site U1592. [Download table in CSV format.](#)

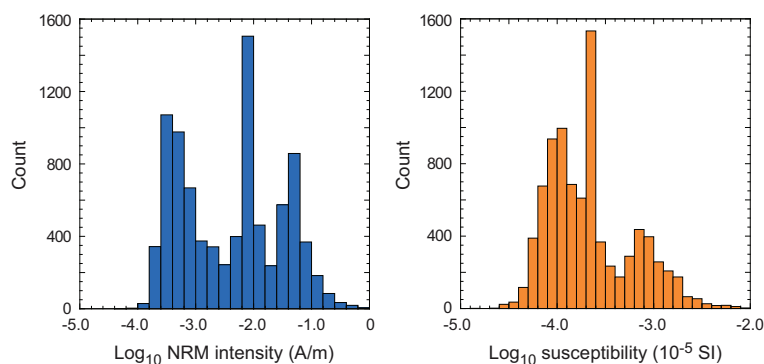


Figure F33. Histograms of NRM intensity and low-field MS, Site U1592. Data are based on archive-half section SRM measurements and low-field point MS measurements made at the same intervals downhole.

alternating field (AF) demagnetization data (after applied fields of 15, 20, and 25 mT) measured at 8787 intervals downhole. Point MS data obtained from the archive-half sections were also filtered to preserve only data corresponding to the intervals where remanence measurements were made. In addition, 61 discrete samples were subject to AF demagnetization in maximum applied fields of up to 50–100 mT (in some cases up to 200 mT) to further constrain magnetic polarities.

Downhole variations in magnetic properties are shown in Figure F34, combining data from Holes U1592A and U1592B. Declinations of magnetizations are azimuthally unconstrained and show wide variations between cores, as expected. Inclinations are observed to become shallower than the NRM directions following demagnetization, reflecting removal of a ubiquitous drilling-induced remanent magnetization. Variations in inclinations fall into two zones: (1) intervals 0–82 mbsf and ~270–348 mbsf have inclinations that are consistently positive and close to the geocentric axial dipole (GAD) expected value of 56° for the site, and (2) a zone below 400 mbsf exhibits systematic variations between normal and reversed inclinations. The significance of these data for magnetostratigraphic dating is discussed below. Median destructive fields throughout the sampled sequence are typically 10–20 mT (Figure F34), indicating dominance of low-coercivity magnetic minerals.

We applied an automated principal component analysis (PCA) approach to analyze archive-half section data acquired at higher AF demagnetization steps to identify samples displaying linear decay toward the origin during demagnetization (see **Paleomagnetism** in the Site U1589 chapter [Druitt et al., 2024]). This involved comparing free-fitting and anchored PCA directions through the 15, 10, and 25 mT step remanences calculated with PuffinPlot software and accepting only those free-fitting PCAs with maximum angular deviations $<15^\circ$ that differ by $<15^\circ$ from the corresponding anchored PCAs. The resulting PCA data set represents the highest quality inclination estimates obtained in each of the holes sampled at Site U1592. We also calculated the Fisher mean directions of the remanences measured in each interval downhole after demagnetization at 15, 20,

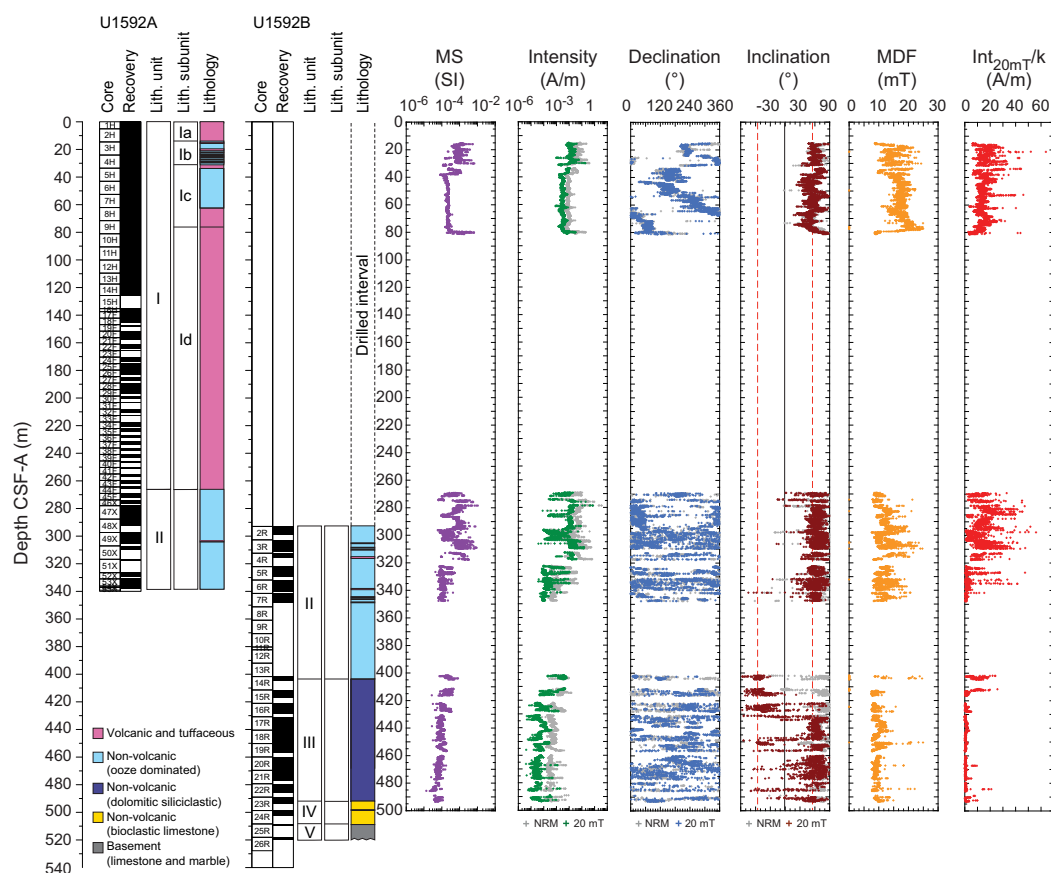


Figure F34. Archive-half section magnetic data, Site U1592. Red dashed lines = GAD inclinations expected at this site.

and 25 mT. For samples where no valid PCA was found, we accepted those Fisher mean directions with precision parameters >15 and α_{95} cones of confidence $<15^\circ$. Samples that yielded neither statistically acceptable PCAs nor Fisher mean directions were represented in the final site database by their 25 mT step inclinations. The combination of these three different estimates of inclinations downhole was then used to define magnetozones.

7.3. Correlations with the geomagnetic polarity timescale

Variations in inclination with depth combining data from both holes into a single record (divided by quality) are shown in Figures F35 and F36, and examples of both archive-half section and discrete sample demagnetization data are shown in Figure F37. The highest quality PCA directions to 348 mbsf have a mean inclination of 57.8° ($k = 18.5$; $\alpha_{95} = 2.6$; $n = 5296$). This agrees well with the GAD field inclination of 56° at Site U1592, confirming that this interval carries a normal polarity magnetization acquired in the Brunhes Chron. However, the Brunhes/Matuyama transition was not recovered at this site.

From 400 to 457 mbsf, inclinations within the dolomitic siliciclastic unit show systematic variations with depth that define three clear reversals that may be correlated with confidence to the geomagnetic polarity timescale (Gradstein et al., 2020) and are consistent with available biostratigraphic markers (see **Biostratigraphy**). Inclination data for this interval are shown in detail in

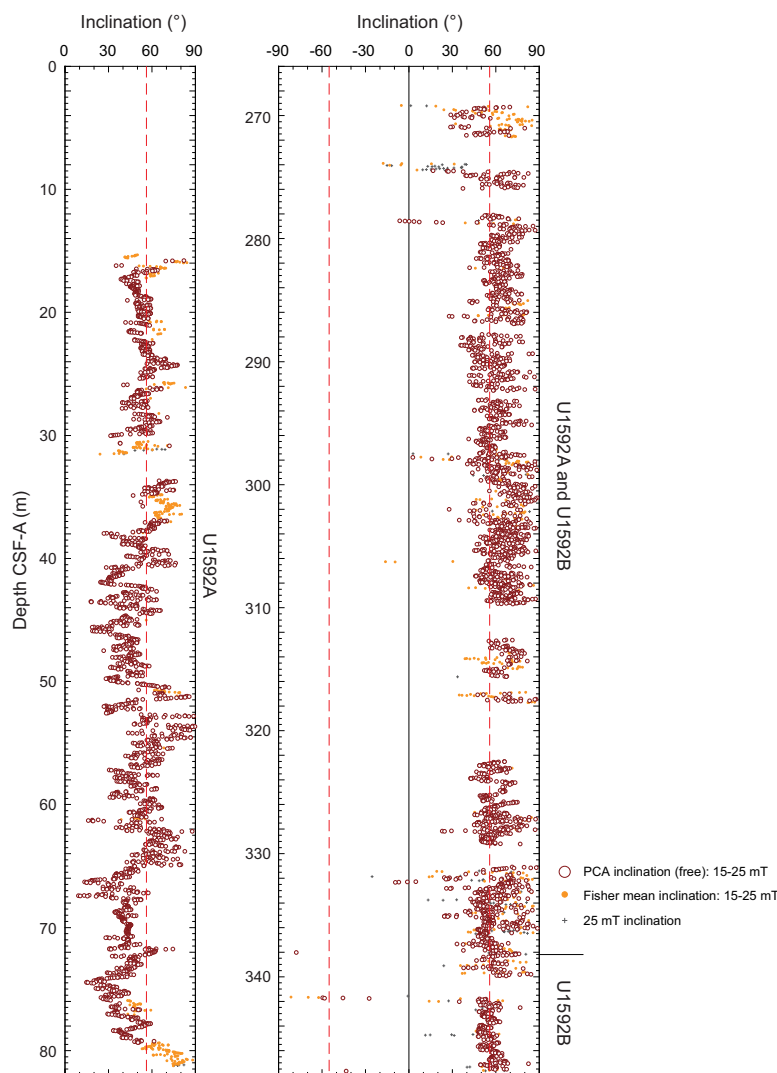


Figure F35. Archive-half section magnetic inclinations, Site U1592. Intervals are correlated to the Brunhes Chron. Red dashed lines = GAD inclinations expected at this site.

Figure F36. Reversals at 431.0 and 449.2 mbsf correlate with the top and base of Chron C1r.1n (Jaramillo Subchron) at 1.008 and 1.076 Ma, respectively (Gradstein et al., 2020). A reversal at 452.0 mbsf correlates with the top of Chron C1r.2n (Cobb Mountain; Gradstein et al., 2020) at 1.189 Ma. A biostratigraphic marker for 1.245 Ma (see [Biostratigraphy](#)) suggests that the base of Chron C1r.2n (1.221 Ma) may be located at 456.5 mbsf, where a narrow interval of negative 25 mT inclinations is seen; however, this is a tentative correlation.

Finally, the lower part of the dolomitic siliciclastic unit shows generally positive inclinations (Figure F36), but these occur in an interval that biostratigraphic markers indicate falls entirely within reversed Chron C1r.3r (Gradstein et al., 2020; see [Biostratigraphy](#)). This suggests that this interval has been remagnetized during either the Jaramillo/Cobb Mountain Subchrons or the Brunhes Chron.

7.4. Anisotropy of low-field magnetic susceptibility

Anisotropy of magnetic susceptibility was measured on 60 discrete samples from Site U1592 (Figure F38). The distribution of the majority of sample minimum principal susceptibility (k_{\min}) axes is subvertical with subhorizontal girdle distributions of intermediate (k_{int}) and maximum (k_{max}) axes. Corrected anisotropy degrees, P_j , reach maximum values of 1.08 (i.e., 8% anisotropy), but the majority of samples have moderate anisotropies of ~ 1.01 – 1.05 . Shape parameters are mainly positive, indicating dominance of oblate anisotropy ellipsoids. These distributions are characteristic of primary depositional fabrics with k_{\min} principal axes oriented normal to bedding.

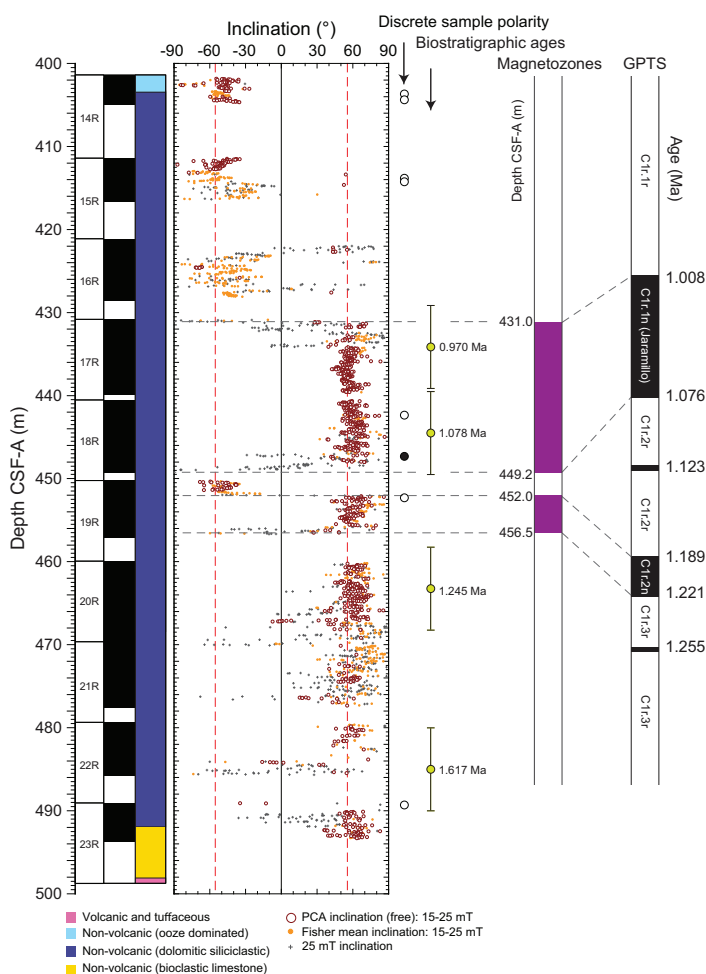


Figure F36. Archive-half section magnetic inclinations for 400–500 mbsf, Site U1592. Data are used to define magnetozones that are correlated to the geomagnetic polarity timescale (GPTS) of Gradstein et al. (2020). Red dashed lines = GAD inclinations expected at this site. Solid/open circles = normal/reversed polarity of discrete samples.

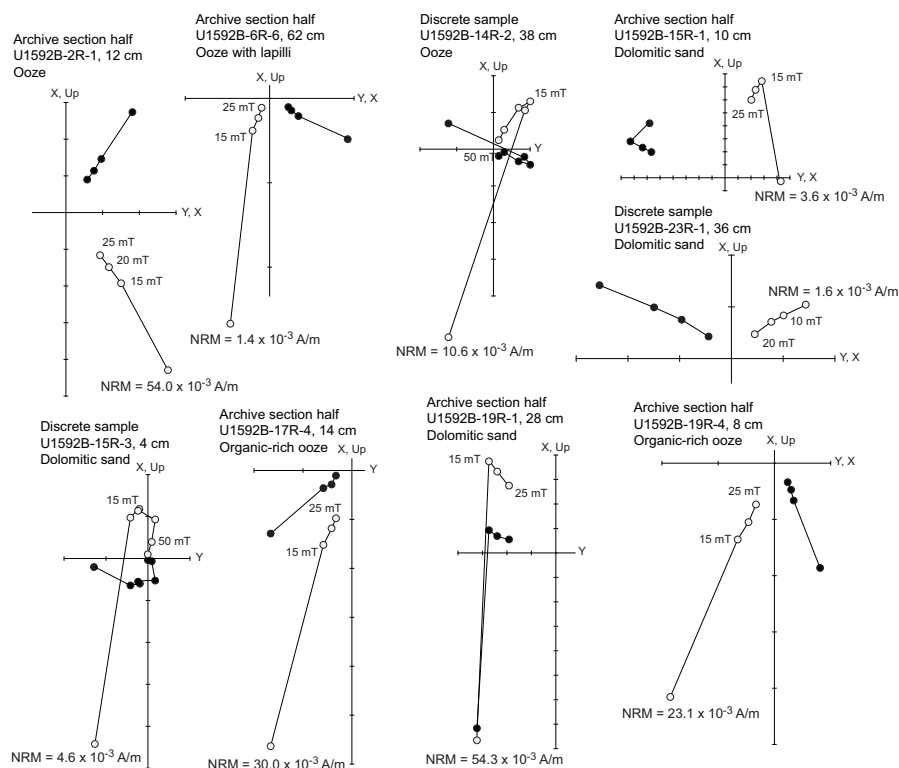


Figure F37. AF demagnetization of discrete samples and archive-half sections, Hole U1592B. Solid circles = projection onto horizontal plane, open circles = projection onto vertical plane.

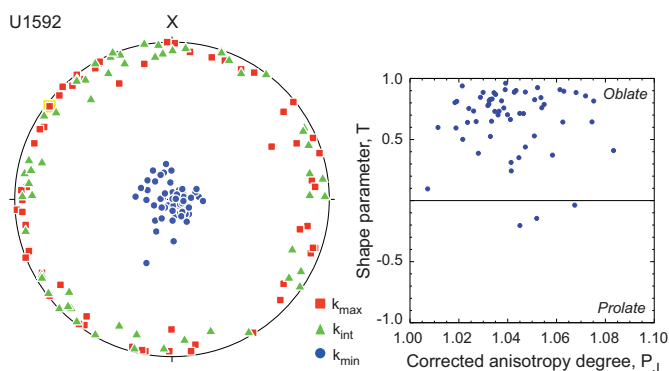


Figure F38. Anisotropy of low-field magnetic anisotropy results from discrete samples, Site U1592. Left: lower hemisphere stereographic equal-area projections of principal anisotropy axes (min = minimum, int = intermediate, max = maximum). Right: shape parameter plotted against corrected anisotropy degree (Jelínek and Kropáček, 1978).

8. Physical properties

Physical properties at Site U1592 are correlated with the respective lithology and lithostratigraphic units. Volcaniclastic Lithostratigraphic Subunit Ia has low NGR counts and high MS relative to other volcaniclastic units. Grain densities are as low as 1.9 g/cm^3 in coarse, pumice-rich deposits. Volcaniclastic layers in Subunit Ic have lower MS, and NGR is a factor of 2 higher than in Subunits Ia and Ib. Subunit Id exhibits large variations in MS; often MS is high compared to other sediments at this site. In Unit II, which is dominated by nannofossil-rich oozes, P -wave velocity increases with depth, NGR is low, and MS is low except where thin volcaniclastic layers have high MS. The dolomitic and siliciclastic layers of Unit III often display cyclic variations in NGR that are correlated with organic-rich layers. Limestones and marbles in Units IV and V have higher P -wave velocity, thermal conductivity, and bulk density and lower NGR than Units I–III.

8.1. Whole-round GRA density, MS, *P*-wave velocity, and NGR

Figure F39 summarizes data collected on whole-round cores measured using the GRA densitometer, MS loop, and *P*-wave logger on the WRMSL as well as NGR. All cited depths are on the CSF-A scale. There are a few possible systematic sources of error in these data that should be considered when interpreting absolute values and trends.

- Redistribution of unconsolidated volcanoclastic materials in core liners during coring and on the core deck can lead to sorting by particle size and density and hence to cyclic changes in physical properties (Figure F40).
- During XCB (Hole U1592A) and RCB (Hole U1592B) coring, recovered cores can contain cracks and void space around the cored materials that lower the values of all physical property measurements made on whole-round cores.
- In Lithostratigraphic Subunits Ic and Id, WRMSL *P*-wave velocity is systematically higher than discrete point measurements (Figure F40). These core sections typically had bubbles on the core liner and expanded end caps.
- The lower *P*-wave velocity measured on split cores may be the result of decompression upon splitting. Whole-round measurements in sections that match discrete measured values on split cores are thus most reliable.
- Whole-round *P*-wave velocity data were not collected for XCB (Hole U1592A) and RCB (Hole U1592B) cores because the cored materials did not fill the core liner.

MS is high in the volcanoclastic deposits at this site. These variations arise from differences in relative abundance of ferromagnetic minerals. For example, MS values in volcanoclastic Subunit Ia in the uppermost 30 m and the cored intervals that contain tuffaceous sand in the lower half of Unit I (200–270 mbsf in Hole U1592A) exceed several hundred $\times 10^{-5}$ SI units. MS is low ($<1 \times 10^{-5}$ SI) in Units III–V.

Care should be taken in assessing MS values in cores from thick, unconsolidated volcanoclastic deposits. The prominent peaks in MS in Subunit Id are often artifacts of coring and recovery, as coarse volcanoclastic materials fall into the tops of the cores. This type of artifact can be recog-

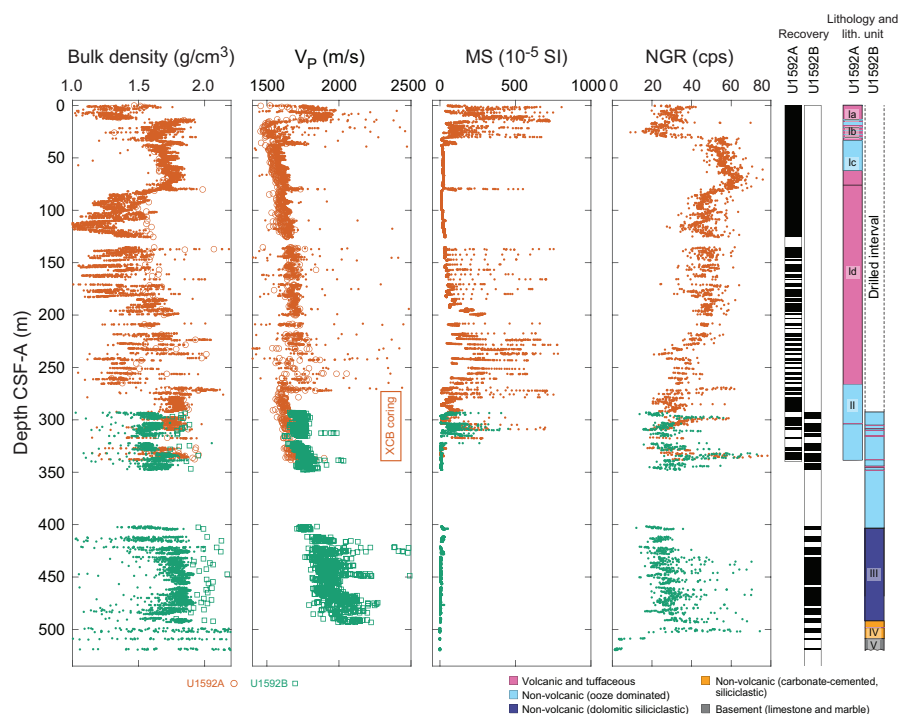


Figure F39. Physical properties, Site U1592. Dots = whole-round measurements, open symbols = discrete sample measurements. Samples with bulk density and *P*-wave velocity greater than the maximum values on the x-axes are plotted in Figure F42. cps = counts per second.

nized by high MS at the top of each core (Figure F40). Recognizing such recovery disturbances provides a guide for assessing other measurements in those cores.

NGR measurements on whole-round core sections show (at least qualitatively) cyclic variations that are most clear in Unit III (Cores 398-U1592B-17R through 22R; 430–490 mbsf). Variations are often correlated with the presence of organic-rich lithologies (Figure F41; see **Lithostratigraphy**). NGR measurements from Unit V Cores 25R and 26R (508–520 mbsf) show distinctive decreases from ~30 to <4 counts/s with increasing depth (Figure F39).

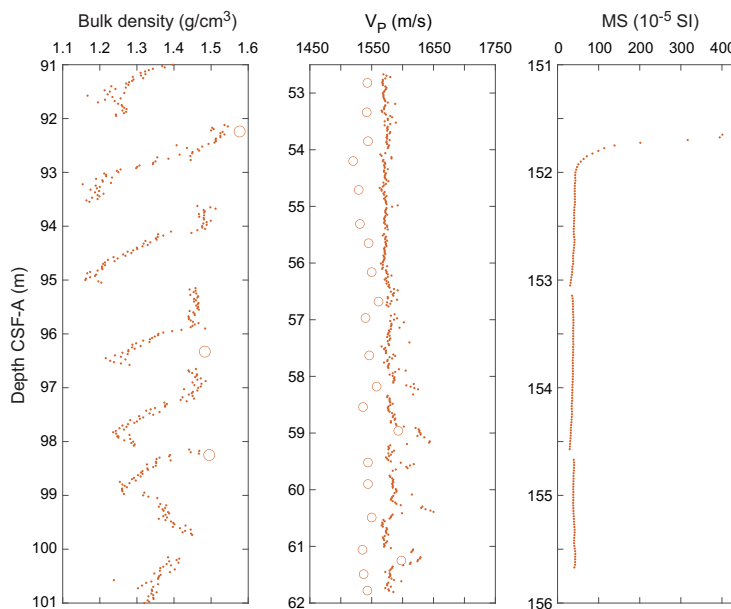


Figure F40. Coring disturbance effects on physical properties, Hole U1592A. Bulk density: points = GRA, circles = moisture and density (MAD). Core 11H shows sediment rearrangement in each section. P -wave velocity (V_p): circles = discrete values. Core 7H shows systematic offset from expansion after the cores are split. MS: Core 20F shows high-MS material falling into the top of recovered cores.

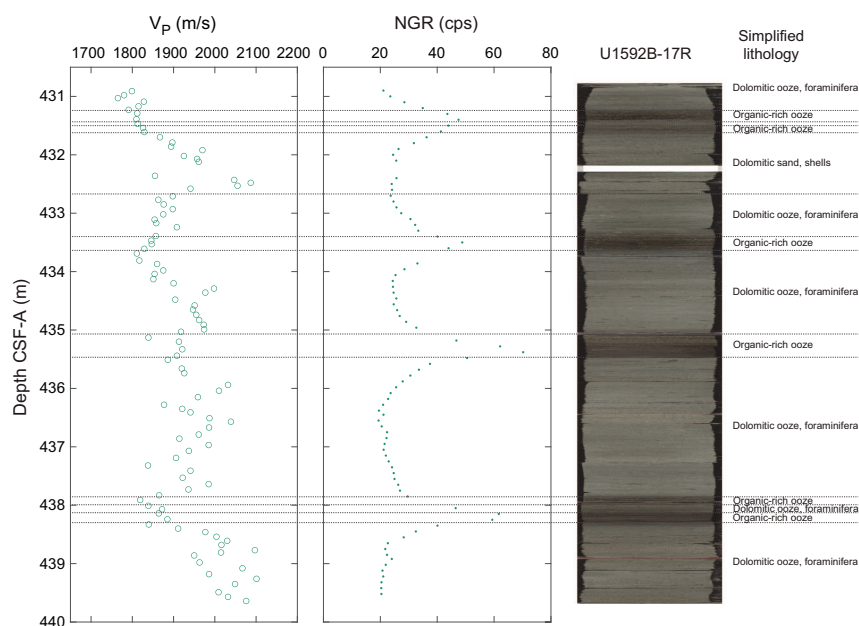


Figure F41. Section showing relationships between discrete P -wave velocity, whole-round NGR, and lithology, Hole U1592B. Uppermost and lowermost NGR measurements are removed from each section because the values are affected by edges of core liners. White bar on image = void space where IW samples were collected. cps = counts per second.

8.2. Discrete measurements

8.2.1. Material strength

Sediment strength was measured with a pocket penetrometer on the catwalk immediately after section splitting. Automated vane shear (AVS) strength measurements were made on working-half sections. A total of 21 AVS measurements were made on working-half sections from 13 to 162 mbsf in Hole U1592A (Figure F42; Table T11). A plunger was used to pack sediment in sections between 136 and 162 mbsf and, thus, the AVS measurements capture reconstituted materials at these depths. A total of 15 pocket penetrometer measurements were made (Table T11) on fine-grained materials in Hole U1592A that remained intact in core liners upon recovery on the catwalk. No measurements were made in Hole U1592B during RCB coring because the recovered material was too stiff or was already crumbling during splitting of the core sections. Figure F42 shows that below 200 mbsf, shear strength increases as a function of depth to 336 mbsf. At still greater depths, fine-grained sediment became too stiff to be measured.

8.2.2. P-wave velocity

Totals of 726 and 1144 discrete *P*-wave velocity measurements were conducted on Hole U1592A and U1592B working-half sections, respectively. *P*-wave velocity in these sections follows the overall trend observed by WRMSL measurements on whole-round cores to the end of APC coring operations in Core 398-U1592A-45F (Figure F39; Table T12). *P*-wave velocity of the nonvolcanic oozes in Lithostratigraphic Subunit Ic increases with depth from ~1.6 to ~1.8 km/s. A thin sandy layer in the dolomitic siliciclastic Unit III has *P*-wave velocity reaching 3.0 km/s, higher than sediment layers above and below (Cores 398-U1592B-15R and 16R). Overall, *P*-wave velocity increases with depth throughout Units I–III, which is expected as formations compact. Marble in Unit V has the highest *P*-wave velocities at this site, reaching 6.5 km/s.

P-wave measurements on working-half sections from Cores 398-U1592A-49X through 55X and 398-U1592B-2R through 7R identify coring disturbance that affects discrete *P*-wave measurements that led to the lower values in XCB cores (Figure F39). XCB coring can create micro-

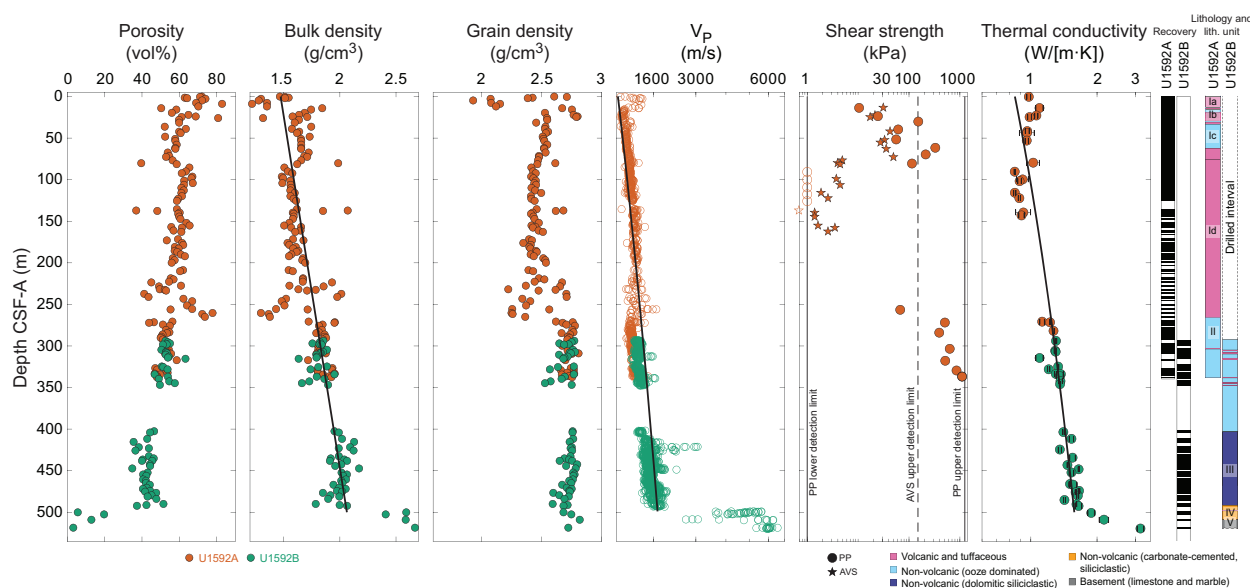


Figure F42. Discrete physical properties measurements, Site U1592. Shear strength: open symbols = measurements outside the instrument range. Sediment below measurements shown was too stiff for measurement. Bulk density and thermal conductivity: linear least-squares fits include the uppermost 499 m. *P*-wave: fit is to data in the uppermost 499 m excluding XCB cores.

Table T11. Shear strength, Site U1592. [Download table in CSV format.](#)

Table T12. *P*-wave velocity, Site U1592. [Download table in CSV format.](#)

fractures, which reduce seismic velocities. At this site, XCB cores also had biscuiting, a drilling disturbance in which soft, low-seismic velocity material that originated from drilling is found between the coherent center of the cores and the surrounding core liner. With ~100 m/s difference between velocities from XCB and RCB cores, Hole U1592A *P*-wave velocity values (~1.6 km/s) in this cored interval are systematically lower than those of Hole U1592B (~1.7 km/s). There are thus two not mutually exclusive origins for the discrepancies between velocities in Holes U1592A and U1592B: (1) low-velocity mud enveloping XCB cores and (2) microfracturing of cored materials from ring shear stress during XCB coring.

Discrete measurements should in general be more reliable and have less scatter than WRMSL measurements because the caliper method measures *P*-wave velocity of cored materials by direct contact. In contrast, WRMSL measures material in core liners that contain water pockets, fractures, and other gaps that are ubiquitous in the XCB and RCB cores that dominated drilling operations at Site U1592. However, data from Site U1592 highlight the effects of sediment expansion (Figure F40), XCB microfracturing, and other coring disturbances (Figure F39) on discrete *P*-wave velocity measurements.

A least-squares fit to measurements in the uppermost 499 mbsf from Holes U1592A and U1592B, excluding XCB cores from Hole U1592A and data from Units IV and V in Hole U1592B (a total of 1638 discrete measurements), gives

$$\text{velocity } (z) = (1.421 \pm 0.020) + (1.315 \pm 0.056)z \text{ km/s,}$$

where *z* is in kilometers and reported \pm values are standard errors.

8.2.3. Moisture and density

Totals of 124 and 59 discrete samples were collected from Holes U1592A and U1592B, respectively, to conduct moisture and density measurements (Figure F42; Table T13). Bulk density derived by measurements on discrete samples should be more reliable than GRA density data from WRMSL measurements on whole-round cores.

Porosity ranges 3–83 vol% (mean = 54 vol%; standard deviation = 11 vol%). Bulk density ranges 1.2–2.7 g/cm³ and is lowest in volcanoclastic materials with the highest porosity. Bulk density increases with depth. A least-squares fit of bulk density data from Units I–III in the uppermost 499 m is

$$\rho(z) = (1.472 \pm 0.022) + (1.181 \pm 0.077)z \text{ g/cm}^3,$$

where *z* is in kilometers and reported \pm values are standard errors.

Grain density varies 1.9–2.8 g/cm³ (mean = 2.59 g/cm³; median = 2.65 g/cm³) with the lowest values in volcanoclastic subunits in the uppermost 280 m.

8.2.4. Thermal conductivity

A total of 47 thermal conductivity measurements were made on selected working-half sections, typically 1 or 2 per core (Table T14). Overall, thermal conductivity increases with increasing depth (Figure F42), as expected from the compaction of sediments. In the uppermost 150 m, however, there is no systematic change of thermal conductivity with depth. The limestones and marbles in Units IV and V have higher thermal conductivities (>2 W/[m·K]) than other sediments at similar depths (1–2 W/[m·K]). A least-squares linear fit to the thermal conductivity data for the uppermost 499 m (omitting the high values from basement and near-basement rocks) is

$$k(z) = (0.847 \pm 0.030) + (1.46 \pm 0.09)z \text{ W/(m·K),}$$

where *z* is in kilometers and reported \pm values are standard errors.

Table T13. Moisture and density (MAD) measurements, Site U1592. [Download table in CSV format.](#)

Table T14. Thermal conductivity, Site U1592. [Download table in CSV format.](#)

9. Geochemistry

9.1. Volcaniclastic bulk geochemistry

To determine the geochemistry of the volcanic and tuffaceous materials, nine tephra and ash samples were handpicked from various layers in Hole U1592A. Following cleaning, grinding, fusion, and dissolution, the materials were analyzed shipboard for major (Si, Al, Fe, Mg, and Ca), minor (Ti, Mn, Na, K, and P), and trace (Sc, V, Cr, Co, Ni, Cu, Zn, Rb, Sr, Y, Zr, Nb, Ba, Ce, and Nd) elements using inductively coupled plasma–atomic emission spectroscopy (ICP-AES) (see **Geochemistry** in the Expedition 398 methods chapter [Kutterolf et al., 2024] for analytical technique). Several unknown samples were run multiple times to determine analytical reproducibility.

9.1.1. ICP-AES: major, minor, and trace elements

Of the volcaniclastic units sampled, two were classified as basaltic andesites, two as trachyandesites, and five as dacites or trachydacites (Table T15; Figure F43). Bulk chemistry values are less evolved than glass chemistry reported in Kutterolf et al. (2021), as expected due to bulk analyses including both minerals and glass.

Concentrations are reported for all analyzed trace elements, but Ce, Cr, Cu, Nb, Ni, P, Rb, S, and V were below detection limits in the majority of samples and are not shown for respective samples in Table T15; volcaniclastic analytical errors are $\pm 1\%$ for major elements and $\pm 5\%$ – 10% for trace elements (see **Geochemistry** in the Expedition 398 methods chapter [Kutterolf et al., 2024]). Trace element ratios were used to broadly discriminate between the volcanic centers of Kolumbo, Santorini, and Christiana.

9.2. Interstitial water geochemistry

To determine the inorganic constituents of IW, a total of 32 water samples were taken from the mudline and whole-round squeezing of sediment intervals from Holes U1592A (19 samples) and

Table T15. ICP-AES data for major, minor, and trace elements, Hole U1592A. [Download table in CSV format.](#)

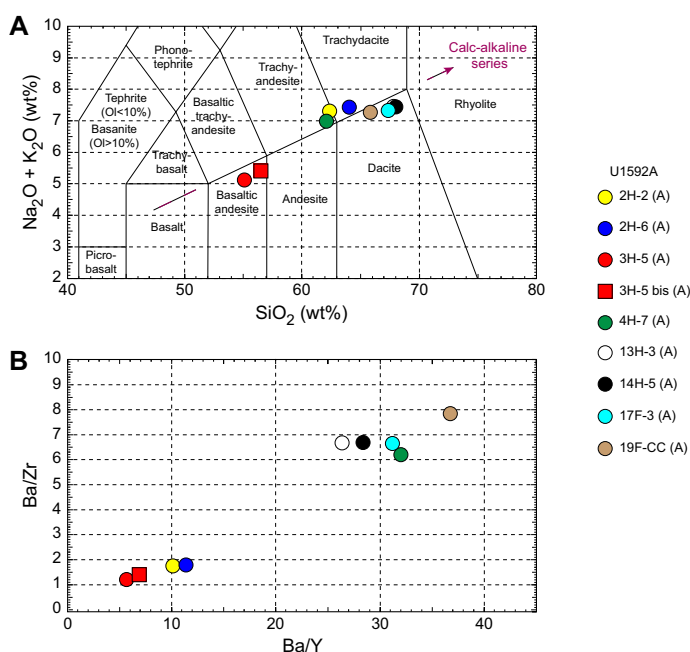


Figure F43. ICP-AES analyses of selected volcaniclastic units used to discriminate between potential volcanic sources, Hole U1592A. A. Total alkali vs. SiO₂ plot with the rock nomenclature of Le Maitre et al. (2002) overlain used for sample naming. Ol = olivine. B. Ba/Y vs. Ba/Zr plot used to correlate samples.

U1592B (13 samples). Aliquots of IW were used for shipboard analyses, and the remaining water was taken for shore-based analysis, following protocols specified by individual scientists. The retrieved pore waters were analyzed shipboard for salinity, alkalinity, pH, major anions (Cl^- , SO_4^{2-} , and Br^-), major cations (Ca^{2+} , Na^+ , Mg^{2+} , and K^+), and major (S, Ca, Mg, K, and Na) and minor (B, Ba, Fe, Li, Mn, P, Si, and Sr) elements using the methods described in **Geochemistry** in the Expedition 398 methods chapter (Kutterolf et al., 2024).

9.2.1. Salinity, alkalinity, and pH

Salinity ranges 30–58 throughout the hole; most values fall between 34 and 44 (Table **T16**; Figure **F44**). The highest salinity value of 58 was recorded near the base of Hole U1592B (Section 23R-2; 491.39 mbsf). Salinities less than 39 may be related to pore water freshening from the dehydration of clays at depth or during the squeezing procedure.

Alkalinity slightly increases (2.5–7.0 mM) to 38 mbsf in Hole U1592A, followed by a decrease with depth to the base of the hole (Table **T16**; Figure **F44**). In Hole U1592B, alkalinity decreases with depth from 313 mbsf (3.6 mM) to 455.31 mbsf (1.2 mM). Alkalinity then increases to the base of the hole at 491 mbsf (2.7 mM) (Table **T16**; Figure **F44**).

Values for pH show variation in the sampled depths and range 7.6–8.0 (average = 7.8 ± 0.1), with slightly higher pH recorded in deeper samples in Hole U1592B (Table **T16**; Figure **F44**).

9.2.2. Bromide, chloride, boron, sodium, potassium, magnesium, calcium, and sulfate

Bromide, Cl^- , B, Na^+ , and K^+ follow similar trends to salinity (Table **T17**; Figure **F45**). Calcium, Mg^{2+} , and SO_4^{2-} correlate well with each other and increase in the lowermost 75 m as salinity also increases. However, all three initially decrease in the uppermost 28 m before increasing again where salinity, Br^- , Cl^- , B, and Na^+ remain relatively constant. Minima in Ca^{2+} , Mg^{2+} , and SO_4^{2-} occur at 326–345 and 432 mbsf, and a local maximum occurs at 414 mbsf.

9.2.3. Lithium, strontium, manganese, barium, and silicon

Trends for Li, Sr, Mn, Ba, and Si do not follow salinity trends (Table **T17**; Figure **F46**). Lithium concentrations increase two orders of magnitude in the uppermost 101 m (from 31 to 1429 μM). Below 275 mbsf, Li shows two small troughs at much lower concentrations than the maximum above. Strontium increases with depth and reaches its highest concentrations near 465 mbsf. Ba

Table T16. Alkalinity, pH, and salinity values, Site U1592. [Download table in CSV format.](#)

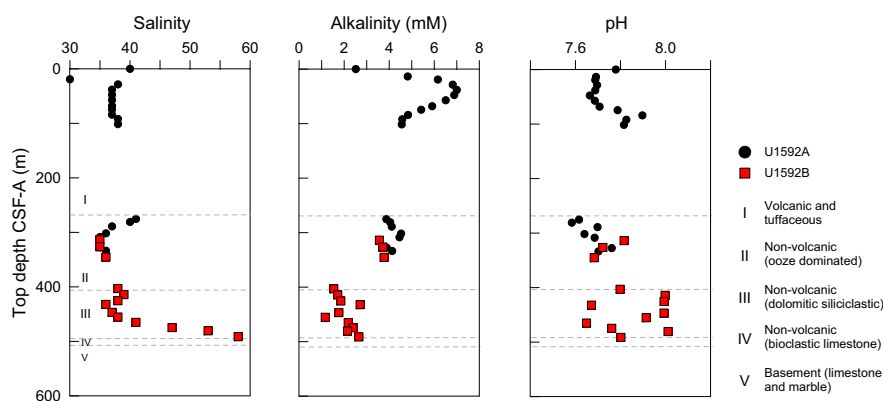


Figure F44. IW salinity, alkalinity, and pH, Site U1592. Dashed lines = unit boundaries.

Table T17. IW data for major anions and cations measured using ion chromatography and major and minor elements measured using ICP-AES, Site U1592. [Download table in CSV format.](#)

concentrations have a clear peak between 275 and 345 mbsf, reaching 14 μM at 326 mbsf. Manganese concentrations are elevated at 0–47 and 275–308 mbsf. IW Si concentrations increase to a maximum of 820 μM at 57 mbsf. Below this, Si decreases with depth with some scatter. Iron and phosphorus were below the detection limit in all but five and two samples in Holes U1592A and U1592B, respectively, and thus are not plotted.

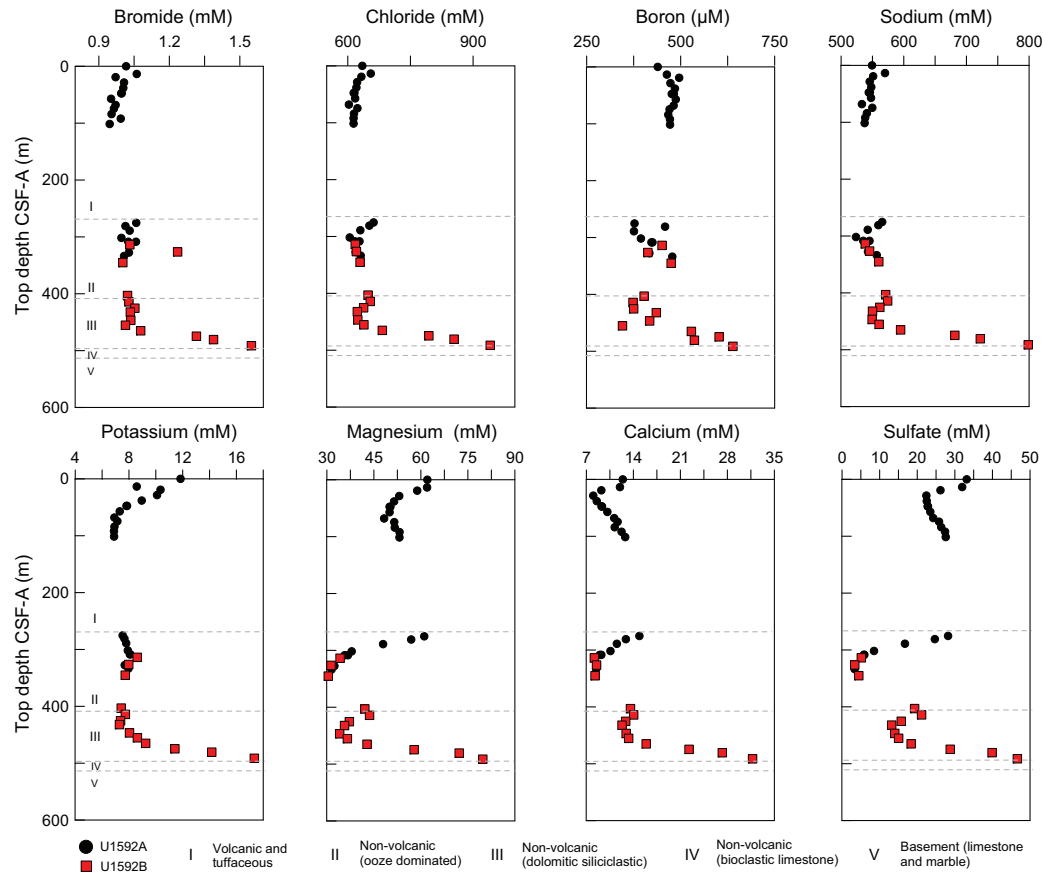


Figure F45. IC and ICP-AES concentrations of Br, Cl, B, Na, K, Mg, Ca, and SO_4^{2-} in IW samples, Site U1592. Dashed lines = unit boundaries.

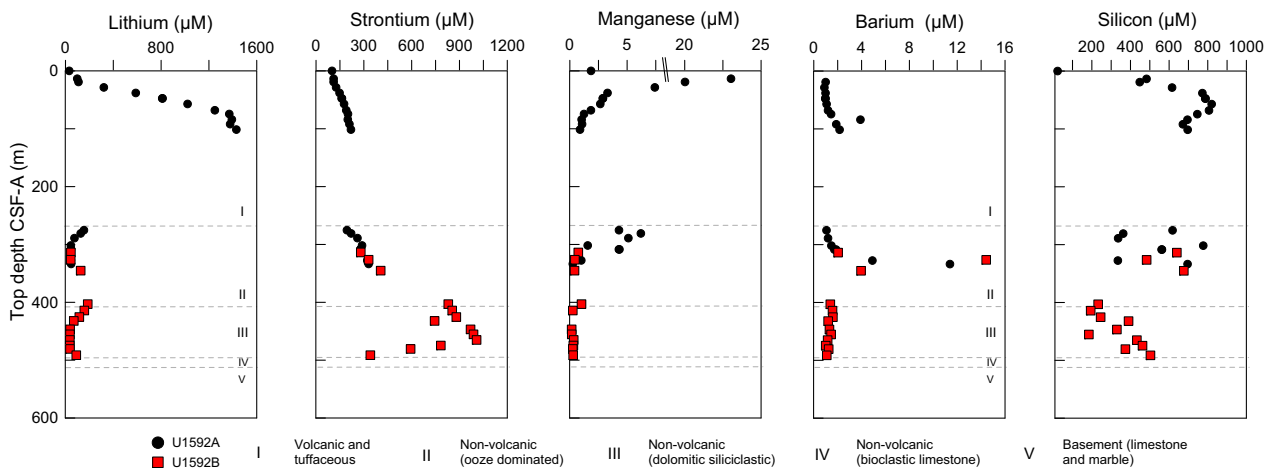


Figure F46. ICP-AES concentrations of Li, Sr, Mn, Ba, and Si in IW samples, Site U1592. Dashed lines = unit boundaries.

9.3. Sediment bulk geochemistry

A total of 31 sediment samples were analyzed for bulk geochemistry (Table T18). All 31 were analyzed for total carbon, hydrogen, and nitrogen (CHN), and 16 were analyzed for inorganic carbon and carbonate content following the protocols explained in **Geochemistry** in the Expedition 398 methods chapter (Kutterolf et al., 2024). For CHN analysis, duplicates were run for ~10% of the samples to determine analytical reproducibility (standard deviation: N = 0.01; C = 0.08). Both carbonate and total organic carbon (TOC) decline from 19 to 101 mbsf. The highest carbonate values are noted below 283 mbsf, where values reach 58 wt% (Figure F47).

9.3.1. Sapropel identification

TOC was calculated using total carbon and inorganic carbon values. Following the convention set forth by Kidd et al. (1978), units with TOC values >2.0 wt% were identified as sapropels and units with TOC values of 0.5–2.0 wt% were identified as sapropelitic. Using these values, six units were identified as sapropelitic (Figure F47).

9.4. Headspace gas analysis

Headspace gas analyses were performed at a resolution of one sample per full-length core (9.5 m advance) or one sample every other core for half-length cores (4.7 m advance) throughout Hole U1592A. The aim was to monitor the presence and abundance of C₁–C₃ hydrocarbons as part of the standard IODP safety protocol (Pimmel and Claypool, 2001). A total of 40 headspace gas samples from this hole were analyzed using gas chromatography (GC) (see **Geochemistry** in the Expedition 398 methods chapter [Kutterolf et al., 2024]). Methane, ethane, and propane concentrations were below the detection limit throughout Hole U1592A.

Headspace gas analyses were resumed on Hole U1592B when coring reached deeper than Hole U1592A (345.27 mbsf). Below this depth, headspace gas analyses were performed at a resolution of one sample per core or one sample every other core for half-length cores to the base of the hole. A total of 11 headspace gas samples were analyzed using GC. Methane, ethane, and propane concentrations were below the detection limit throughout Hole U1592B. Headspace gas values are not shown in a figure because they were below the detection limit in all measured samples.

Table T18. Total inorganic carbon, percent CaCO₃, TC, TN, and TOC data, Site U1592. [Download table in CSV format.](#)

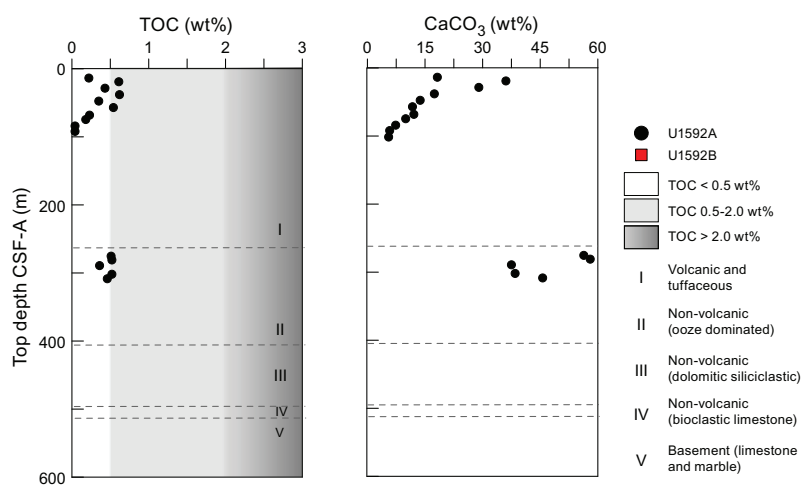


Figure F47. TOC and carbonate, Site U1592. Dashed lines = unit boundaries. Sapropel units follow convention from Kidd et al. (1978).

References

- Aze, T., Ezard, T.H.G., Purvis, A., Coxall, H.K., Stewart, D.R.M., Wade, B.S., and Pearson, P.N., 2011. A phylogeny of Cenozoic macroperforate planktonic foraminifera from fossil data. *Biological Reviews*, 86(4):900–927. <https://doi.org/10.1111/j.1469-185X.2011.00178.x>
- Backman, J., Raffi, I., Rio, D., Fornaciari, E., and Pälke, H., 2012. Biozonation and biochronology of Miocene through Pleistocene calcareous nannofossils from low and middle latitudes. *Newsletters on Stratigraphy*, 45(3):221–244. <https://doi.org/10.1127/0078-0421/2012/0022>
- Crundwell, M., Scott, G., Naish, T., and Carter, L., 2008. Glacial–interglacial ocean climate variability from planktonic foraminifera during the mid-Pleistocene transition in the temperate southwest Pacific, ODP Site 1123. *Palaeogeography, Palaeoclimatology, Palaeoecology*, 260(1–2):202–229. <https://doi.org/10.1016/j.palaeo.2007.08.023>
- Crundwell, M.P., and Woodhouse, A., 2022. A detailed biostratigraphic framework for 0–1.2 Ma Quaternary sediments of north-eastern Zealandia. *New Zealand Journal of Geology and Geophysics*. <https://doi.org/10.1080/00288306.2022.2054828>
- Di Stefano, A., and Sturiale, G., 2010. Refinements of calcareous nannofossil biostratigraphy at the Miocene/Pliocene Boundary in the Mediterranean region. *Geobios*, 43(1):5–20. <https://doi.org/10.1016/j.geobios.2009.06.007>
- Druitt, T., Kutterolf, S., and Höfig, T.W., 2022. Expedition 398 Scientific Prospectus: Hellenic Arc Volcanic Field. International Ocean Discovery Program. <https://doi.org/10.14379/iodp.sp.398.2022>
- Druitt, T.H., Kutterolf, S., Ronge, T.A., Beethe, S., Bernard, A., Berthod, C., Chen, H., Chiyonobu, S., Clark, A., DeBari, S., Fernandez Perez, T.I., Gertisser, R., Hübscher, C., Johnston, R.M., Jones, C., Joshi, K.B., Kletetschka, G., Koukousioura, O., Li, X., Manga, M., McCanta, M., McIntosh, I., Morris, A., Nomikou, P., Pank, K., Peccia, A., Polymenakou, P.N., Preine, J., Tominaga, M., Woodhouse, A., and Yamamoto, Y., 2024. Site U1589. In Druitt, T.H., Kutterolf, S., Ronge, T.A., and the Expedition 398 Scientists, Hellenic Arc Volcanic Field. Proceedings of the International Ocean Discovery Program, 398: College Station, TX (International Ocean Discovery Program). <https://doi.org/10.14379/iodp.proc.398.103.2024>
- Dunham, R.J., 1962. Classification of carbonate rocks according to depositional texture. In Ham, W.E., *Classification of Carbonate Rocks*. AAPG Memoir, 1: 108–121.
- Fisher, R.V., and Schmincke, H.-U., 1984. *Pyroclastic Rocks*: Berlin (Springer). <https://doi.org/10.1007/978-3-642-74864-6>
- Folk, R.L., 1959. Practical petrographic classification of limestones. *AAPG Bulletin*, 43(1):1–38. <https://doi.org/10.1306/0BDA5C36-16BD-11D7-8645000102C1865D>
- Gradstein, F.M., Ogg, J.G., Schmitz, M.D., and Ogg, G.M. (Eds.), 2020. *The Geologic Time Scale 2020*: Amsterdam (Elsevier BV). <https://doi.org/10.1016/C2020-1-02369-3>
- Hayward, B.W., Grenfell, H.R., Reid, C.M., and Hayward, K.A., 1999. Recent New Zealand shallow-water benthic foraminifera: taxonomy, ecologic distribution, biogeography, and use in paleoenvironmental assessment. In *Institute of Geological & Nuclear Sciences Monograph*, 21: Lower Hutt, NZ.
- Hooft, E.E.E., Nomikou, P., Toomey, D.R., Lampridou, D., Getz, C., Christopoulou, M.-E., O'Hara, D., Arnoux, G.M., Bodmer, M., Gray, M., Heath, B.A., and VanderBeek, B.P., 2017. Backarc tectonism, volcanism, and mass wasting shape seafloor morphology in the Santorini–Christiana–Amorgos region of the Hellenic Volcanic Arc. *Tectonophysics*, 712–713:396–414. <https://doi.org/10.1016/j.tecto.2017.06.005>
- Hübscher, C., Ruhnu, M., and Nomikou, P., 2015. Volcano-tectonic evolution of the polygenetic Kolumbo submarine volcano/Santorini (Aegean Sea). *Journal of Volcanology and Geothermal Research*, 291:101–111. <https://doi.org/10.1016/j.jvolgeores.2014.12.020>
- Jelínek, V., and Kropáček, V., 1978. Statistical processing of anisotropy of magnetic susceptibility measured on groups of specimens. *Studia Geophysica et Geodaetica*, 22(1):50–62. <https://doi.org/10.1007/BF01613632>
- Jutzeler, M., White, J.D.L., Talling, P.J., McCanta, M., Morgan, S., Le Friant, A., and Ishizuka, O., 2014. Coring disturbances in IODP piston cores with implications for offshore record of volcanic events and the Missoula megafloods. *Geochemistry, Geophysics, Geosystems*, 15(9):3572–3590. <https://doi.org/10.1002/2014GC005447>
- Kidd, R.B., Cita, M.B., and Ryan, W.B.F., 1978. Stratigraphy of eastern Mediterranean sapropel sequences recovered during DSDP Leg 42A and their paleoenvironmental significance. In Hsü, K., Montadert, L., et al., *Initial Reports of the Deep Sea Drilling Project*. 42(1): Washington, DC (US Government Printing Office), 421–443. <https://doi.org/10.2973/dsdp.proc.42-1.113-1.1978>
- Kutterolf, S., Druitt, T.H., Ronge, T.A., Beethe, S., Bernard, A., Berthod, C., Chen, H., Chiyonobu, S., Clark, A., DeBari, S., Fernandez Perez, T.I., Gertisser, R., Hübscher, C., Johnston, R.M., Jones, C., Joshi, K.B., Kletetschka, G., Koukousioura, O., Li, X., Manga, M., McCanta, M., McIntosh, I., Morris, A., Nomikou, P., Pank, K., Peccia, A., Polymenakou, P.N., Preine, J., Tominaga, M., Woodhouse, A., and Yamamoto, Y., 2024. Expedition 398 methods. In Druitt, T.H., Kutterolf, S., Ronge, T.A., and the Expedition 398 Scientists, Hellenic Arc Volcanic Field. Proceedings of the International Ocean Discovery Program, 398: College Station, TX (International Ocean Discovery Program). <https://doi.org/10.14379/iodp.proc.398.102.2024>
- Kutterolf, S., Freundt, A., Hansteen, T.H., Dettbarn, R., Hampel, F., Sievers, C., Wittig, C., Allen, S.R., Druitt, T.H., McPhie, J., Nomikou, P., Pank, K., Schindlbeck-Belo, J.C., Wang, K.-L., Lee, H.-Y., and Friedrichs, B., 2021. The medial offshore record of explosive volcanism along the central to eastern Aegean Volcanic Arc: 1. tephrostratigraphic correlations. *Geochemistry, Geophysics, Geosystems*, 22(12):e2021GC010010. <https://doi.org/10.1029/2021GC010010>
- Le Maitre, R.W., Steckeisen, A., Zanettin, B., Le Bas, M.J., Bonin, B., and Bateman, P. (Eds.), 2002. *Igneous Rocks: A Classification and Glossary of Terms* (Second edition): Cambridge, UK (Cambridge University Press). <https://doi.org/10.1017/CBO9780511535581>

- Lirer, F., Foresi, L.M., Iaccarino, S.M., Salvatorini, G., Turco, E., Cosentino, C., Sierro, F.J., and Caruso, A., 2019. Mediterranean Neogene planktonic foraminifer biozonation and biochronology. *Earth-Science Reviews*, 196:102869. <https://doi.org/10.1016/j.earscirev.2019.05.013>
- Maltman, A.J., 1998. Deformation structures from the toes of active accretionary prisms. *Journal of the Geological Society (London, UK)*, 155(4):639–650. <https://doi.org/10.1144/gsjgs.155.4.0639>
- Maltman, A.J., Byrne, T., Karig, D.E., and Lallemand, S., 1993. Deformation at the toe of an active accretionary prism: synopsis of results from ODP Leg 131, Nankai, SW Japan. *Journal of Structural Geology*, 15(8):949–964. [https://doi.org/10.1016/0191-8141\(93\)90169-B](https://doi.org/10.1016/0191-8141(93)90169-B)
- Martini, E., 1971. Standard Tertiary and Quaternary calcareous nannoplankton zonation. *Proceedings of the Second Planktonic Conference, Roma, 1970*:739–785.
- Nomikou, P., Hübscher, C., Papanikolaou, D., Farangitakis, G.P., Ruhнау, M., and Lampridou, D., 2018. Expanding extension, subsidence and lateral segmentation within the Santorini - Amorgos basins during Quaternary: implications for the 1956 Amorgos events, central - south Aegean Sea, Greece. *Tectonophysics*, 722:138–153. <https://doi.org/10.1016/j.tecto.2017.10.016>
- Nomikou, P., Hübscher, C., Ruhнау, M., and Bejelou, K., 2016. Tectono-stratigraphic evolution through successive extensional events of the Anydros Basin, hosting Kolumbo volcanic field at the Aegean Sea, Greece. *Tectonophysics*, 671:202–217. <https://doi.org/10.1016/j.tecto.2016.01.021>
- Okada, H., and Bukry, D., 1980. Supplementary modification and introduction of code numbers to the low-latitude coccolith biostratigraphic zonation (Bukry, 1973; 1975). *Marine Micropaleontology*, 5(3):321–325. [https://doi.org/10.1016/0377-8398\(80\)90016-X](https://doi.org/10.1016/0377-8398(80)90016-X)
- Pimmel, A., and Claypool, G., 2001. Introduction to shipboard organic geochemistry on the JOIDES Resolution. *Ocean Drilling Program Technical Note*, 30. <https://doi.org/10.2973/odp.tn.30.2001>
- Preine, J., Hübscher, C., Karstens, J., and Nomikou, P., 2022a. Volcano-tectonic evolution of the Christiana-Santorini-Kolumbo rift zone. *Tectonics*, 41(11):e2022TC007524. <https://doi.org/10.1029/2022TC007524>
- Preine, J., Karstens, J., Hübscher, C., Nomikou, P., Schmid, F., Crutchley, G.J., Druitt, T.H., and Papanikolaou, D., 2022b. Spatio-temporal evolution of the Christiana-Santorini-Kolumbo volcanic field, Aegean Sea. *Geology*, 50(1):96–100. <https://doi.org/10.1130/G49167.1>
- Rio, D., Raffi, I., and Villa, G., 1990. Pliocene-Pleistocene calcareous nannofossil distribution patterns in the western Mediterranean. In Kastens, K.A., Mascle, J., et al., *Proceedings of the Ocean Drilling Program, Scientific Results*. 107: College Station, TX (Ocean Drilling Program), 513–533. <https://doi.org/10.2973/odp.proc.sr.107.164.1990>
- Rochford, E.L., Prior, D.J., Agar, S.M., and Maltman, A., 1995. Microstructural analysis of deformation bands from Site 860, Chile margin. In Lewis, S.D., Behrmann, J.H., Musgrave, R.J., and Cande, S.C. (Eds.), *Proceedings of the Ocean Drilling Program, Scientific Results*. 141: College Station, TX (Ocean Drilling Program). <https://doi.org/10.2973/odp.proc.sr.141.017.1995>
- Schiebel, R., and Hemleben, C., 2017. *Planktic Foraminifers in the Modern Ocean*: Berlin (Springer). <https://doi.org/10.1007/978-3-662-50297-6>
- Tarling, D.H., 1983. *Paleomagnetism: Principles and Applications in Geology, Geophysics and Archaeology*: Dordrecht, Netherlands (Springer). <https://doi.org/10.1007/978-94-009-5955-2>
- Ujii, K., Maltman, A.J., and Sánchez-Gómez, M., 2004. Origin of deformation bands in argillaceous sediments at the toe of the Nankai accretionary prism, southwest Japan. *Journal of Structural Geology*, 26(2):221–231. <https://doi.org/10.1016/j.jsg.2003.06.001>
- Vannucchi, P., and Tobin, H., 2000. Deformation structures and implications for fluid flow at the Costa Rica convergent margin, ODP Sites 1040 and 1043, Leg 170. *Journal of Structural Geology*, 22(8):1087–1103. [https://doi.org/10.1016/S0191-8141\(00\)00027-4](https://doi.org/10.1016/S0191-8141(00)00027-4)
- Woodhouse, A., Procter, F.A., Jackson, S.L., Jamieson, R.A., Newton, R.J., Sexton, P.F., and Aze, T., 2023. Paleocology and evolutionary response of planktonic foraminifera to the mid-Pliocene Warm Period and Plio-Pleistocene bipolar ice sheet expansion. *Biogeosciences*, 20(1):121–139. <https://doi.org/10.5194/bg-20-121-2023>